Measurement of surface heat transfer caused by interaction of sonic jet and supersonic crossflow near injection hole

Ji-Yeul Bae[a†], Jihyuk Kim[b†], Namkyu Lee[c], Hyungmo Bae[b], Hyung Hee Cho[b*]

[a] Agency for Defense Development, Daejeon 305-600, KOREA

[b] Department of Mechanical Engineering, Yonsei University, 50 Yonsei-ro, Seodaemun-gu, Seoul 120-749, KOREA

[c] IBI-4, Forschungszentrum Jülich GmbH, 52425 Jülich, Germany

† Co-first author (These authors are contributed on this paper equally.)

* Corresponding author
Tel. : +82 2 2123 2828
Fax : +82 2 312 2159
E-mail : hhcho@yonsei.ac.kr

Abstract

This paper investigates the surface heat transfer caused by interaction of a jet and a supersonic crossflow near the jet injection hole. A sonic jet with different momentum ratios (J = 0.510, 1.018, 1.477) was injected perpendicularly into a crossflow with a Mach number of 3.0 in a supersonic wind tunnel. Surface temperature through time measured by infrared thermography was used to deduce surface heat flux. In addition, heat transfer coefficients and adiabatic wall temperatures were derived from time histories of surface heat flux and temperature. In order to consider an effect of conduction from the inner hole surface, a three-dimensional energy conservation is considered in the deduction process of the heat flux. As a result, the characteristics of the heat transfer near the hole and the change in the heat transfer with momentum ratios are presented. The separation vortex and recirculation vortex are found to be dominant flow features in terms of the augmentation of the heat transfer. The maximum heat transfer is observed at the immediate vicinity of the hole due to the flow oscillation from a jet-mixing layer. This oscillation resulted in a 390% of augmentation of the heat transfer near the hole compared to the freestream even at the lowest momentum ratio. Also, the augmentation near the hole is more susceptible to change of momentum ratio compared to the augmentation on the overall interaction area.

Keywords: sonic jet, jet and crossflow interaction, IR thermography

Nomenclature

J	= jet-to-freestream momentum ratio
ρ	= density
v	= velocity
γ	= specific heat ratio
p	= pressure
M	= Mach number
q_{cond}	= conductive heat flux
q_{conv}	= convective heat flux
h	= heat transfer coefficient
T	= Temperature
θ	= temperature difference
z	= depth
α	= thermal diffusivity
c	= specific heat capacity
k	= thermal conductivity
t	= time
D	= diameter of injection hole
h_{aug}	= augmentation of heat transfer coefficient
A_{pixel}	= area of a pixel

Subscripts

j	= jet exit property
∞	= freestream property
aw	= adiabatic wall condition
s	= surface property
0	= stagnation condition
h	= injection hole property

1. Introduction

An interaction between a sonic jet and a supersonic crossflow includes complicated flow features, such as flow separation, shock/boundary layer interaction, and a supersonic mixing layer. This flow pattern can be observed in many applications, such as scramjet combustors, fluidic thrust vector controls in rockets, and side control jets installed on missile outer fuselages [1-7]. Due to complex phenomena related to this subject, extensive research has been carried out to study flow structure of jet, mixing characteristics between two fluids, surface pressure distribution, and so on.

A typical flow structure resulting from the interaction of jet and crossflow is well depicted by Ben-Yakar et al. [8] and shown in Fig. 1. Because the normally injected jet acts as an obstacle to the crossflow, a bow shock develops in front of the jet. The under-expanded jet keeps accelerating downstream until it forms a Mach disk. Turning of the jet towards downstream direction is achieved by a barrel shock surrounding the jet plume. A mixing layer between the crossflow past the bow shock and the jet forms a large-scale structure around the trail of the jet. In addition, surface flow structure and heat transfer on the surface are strongly affected by the bow shock. Because of an adverse pressure gradient caused by the bow shock, the crossflow is separated in front of the bow shock. As a result, a separation shock called a 'Lambda shock' forms above the separation region, and an upstream recirculation region develops between the separation region and the injection hole by the pressure gradient around the jet. Two horseshoe vortices originating from these regions move around the injection hole to a downstream, dominating a characteristic of the heat transfer on the surface.

Early researches focused on studying a flow structure caused by the interaction of the sonic jet and supersonic crossflow. Among these, works of Spaid et al. [9-10] were focused on a penetration of the jet and a resulting change in a flow structure using Schileren flow visualizations and pressure measurements. More advanced measurement techniques such as a pressure-sensitive paint (PSP) and a particle image velocimetry (PIV) have enabled a detailed understanding of the flow structure on the surface and the characteristic of the mixing layer between the jet and the crossflow [5,8,11-16]. Researches based on the large eddy simulation (LES) also contributed to an understanding of the flow by capturing the key characteristics of the large-scale structure of the mixing layer [17-20]. The mechanism of formation of counter rotating vortices (CRVs) around the jet has also been well described.

Viti et al. [21] identified six primary vortices: (i) horseshoe vortex, (ii) an upper trailing vortex, (iii) two trailing vortices formed in the separation region and, after of the bow shock wave, (iv) two more trailing vortices that eventually merge together into one single rotational motion. They found that three pairs of trailing counter rotating vortices (the second of iii and iv) merged into the kidney-shaped major CRVs downstream of the hole. M. B. Sun [22, 23] gave an analysis on the formation of trailing CRVs around the transverse jet with direct numerical simulation. The formation mechanism of the surface trailing CVPs are provided with the instantaneous and time-averaged flow structure [22]. They also found that as the flow penetrating the lateral side of the Mach disk where the strong shear condition exists, the baroclinic torque induces upper vorticities in the opposite rotating direction against the major CRVs [23]. A review by Huang [24] comprehensively summarized efforts to understand the flow and mixing characteristics caused by the interaction between the jet and the crossflow.

Although several studies have been carried out in terms of flow structures and mixing characteristics, a little attention has been given to the heat transfer characteristic on the surface near the injected jet. However, this subject is critical in both scramjet combustor and thrust vector control of a missile as their working gases are in high temperature and can induce a high heat transfer to a component. Especially, the surface near the hole is a harsh region where severe heat transferred to a component as the region is affected by an oscillatory behavior of a shock structure [17]. The oscillation is provoked by a pressure fluctuation in the mixing layer when an ejection of the large-scale vortex occurs and results in oscillations of both barrel shock and bow shock. As the shock structure oscillates, the upstream recirculation region and vortices from it change and affect the heat transfer characteristics. Despite the importance of this subject, the number of published literatures related to this are very limited, and the data for designing the system and validating numerical result are insufficient. There are few literature that have studied the heat transfer on the surface where sonic jet injected into supersonic crossflow. Previously, Roberts et al. [25] measured heat transfer characteristics on the surface with a laminar hypersonic crossflow and a sonic jet using a thermo-liquid crystal (TLC) technique. However, TLC remains inactive in the near-hole region affected by the jet. Guelhan et al. [26] and Taguchi et al. [27] also measured heat transfer on a conical body with sonic jet under a hypersonic condition using infrared thermography. However, they utilized the assumption of a one-dimensional conduction on the

surface and data around the hole is omitted. In the surface near the hole, the 1-D conduction assumption is not valid as the sonic jet flows inside the hole and heat transferred through the inner hole surface. Therefore the conduction in this region occurs in a three-dimensional manner. This leads to an additional surface temperature change near the injection hole. Because heat flux is deduced by the temperature change from an initial temperature, a measured heat flux would be different compared to an actual heat flux on the surface. Consequently, an accurate measurement of the heat transfer near the injection hole is required to understand the characteristics of the heat transfer near the injection hole. Therefore, care should be taken in deducing heat flux near the injection hole.

In this study, a heat transfer near the injection hole caused by an interaction of a jet and a supersonic crossflow was measured using an infrared thermography. A sonic jet with different momentum ratios (J = 0.5, 1.0 and 1.5) was injected into a crossflow with Mach number of 3.0 developing through a length of 60 mm from a leading edge of a test plate. Heat flux distribution on the surface was inversely calculated from a time history of temperature measured in 60 Hz with an infrared camera. A three-dimensional finite volume calculation was carried out with measured temperature distribution as a Dirichlet boundary condition. By using this method, a three-dimensional conduction effect from the injection hole is taken into account, and the effect of the oscillatory behavior near the injection hole on the heat transfer is analyzed. The heat transfer results are analyzed in terms of a heat transfer coefficient and an adiabatic wall temperature, derived from the time history of heat flux and wall temperature.

2. Experimental apparatus and procedure

2.1. Intermittent blow-down wind tunnel

The wind tunnel used in this study is same as the one used in the research of Yu et al. [28], and its key components are shown in Fig. 2. It is an intermittent blow-down wind tunnel and flow is supplied from high pressure vessels having 3.0 m^3 of the total volume and 150 bars of the maximum pressure. The flow from the tank goes through a pressure regulator that can control total pressure of the flow within a range of 1 to 15 bars. Total pressure of the flow was maintained at nearly 7 bars during measurements in this research. After the pressure regulator, there is a settling chamber with six mesh

screens and an ideal nozzle designed by method of characteristics with exit diameter of 60 mm. Then, the flow is discharged into a test section with nearly uniform Mach number of 3.0. The test section is a free-jet type with a diffuser; therefore, there are no effect of a boundary layer interaction from the tunnel wall on a test plate inside the test section.

As the wind tunnel is not equipped with an air heater, the temperature of the flow during the test decreases gradually due to a Joule–Thomson effect at pressure vessels and valves. This drop in the temperature drives a heat transfer between the test plate and the flow by maintaining a temperature difference between the flow and a surface of the test plate. However, total temperature of the flow should be accurately measured and synchronized with surface temperature due to this change. Therefore, the total temperature is measured at the settling chamber using an aspiration-type temperature probe with a J-type thermocouple. The data was taken with a NI DAQ, PCI-6259, with a sampling rate of 1,000 Hz and later synchronized with a surface temperature taken with an infrared camera. Total pressures of the main flow and the secondary flow were measured using pressure transducers with a range of 0 to 10 atmospheric pressure and data from them are also taken by PCI-6259. Especially, the momentum ratio of the jet to the crossflow is related to the two readings from the sensors as follows:

$$J = \frac{\rho_j v_j^2}{\rho_\infty v_\infty^2} = \frac{\gamma_j\, p_j M_j^2}{\gamma_\infty\, p_\infty M_\infty^2} = \frac{\gamma_j p_{0,j}\ \left(1+\frac{\gamma-1}{2}M_j^2\right)^{-\frac{\gamma_j}{\gamma_j-1}} M_j^2}{\gamma_\infty\, p_{0,\infty}\left(1+\frac{\gamma-1}{2}M_\infty^2\right)^{-\frac{\gamma_\infty}{\gamma_\infty-1}} M_\infty^2} \quad (1)$$

A typical history of total pressures and temperature of wind tunnel run for 4 seconds is shown in Fig. 3. In addition, the flow conditions for the test at each momentum ratio are summarized in Table. 1.

2.2. Test plate and temperature measurement

A base of the test plate is a single-sided, 10-degree wedge made of a steel with a length of 90 mm and a width of 60 mm as depicted in Fig. 4 (a). A model support leg, also wedge-shaped to reduce a drag and a flow disturbance, incorporates a secondary flow channel for a sonic jet with a throat diameter of 2.5 mm. Center of the injection hole is located 60 mm downstream from a leading edge of the test plate, and the Reynolds number corresponding to this length scale and freestream condition is 1.24 x 10^6. The secondary flow for the sonic jet is by-passed from the main settling chamber and

supplied through a secondary pressure regulator and a settling chamber as depicted in Fig. 2. The momentum ratio of the jet is controlled by changing a total pressure of the jet at the secondary pressure regulator. Inlet diameter for the secondary flow entering the test plate through the support leg is 5 mm to ensure a chocking and sonic injection of the jet at the injection hole.

In this research, a semi-infinite solid approximation should be maintained to measure a surface heat flux from a change in a surface temperature. In order to satisfy this approximation, a Teflon block with a low thermal conductivity was applied near the injection hole as shown in Fig. 4 (b). Thermal conductivity of the material is 0.25 $W \cdot m^2 \cdot s^{-1}$ and its thermal diffusivity is 8.25 x 10^{-8} $m^2 \cdot s$. Thickness of the Teflon block is 5 mm. Maximum duration for a semi-infinite approximation to be valid can be deduced from the equation below describing ratio of temperature deviation from an initial temperature at a depth z and surface at time t, assuming a step input of constant heat flux q_s [29].

$$\frac{\theta_z}{\theta_s} = e^{-(z^*)^2} - \sqrt{\pi} z^* erfc(z^*) \tag{2}$$

$$z^* = \frac{z}{\sqrt{4\alpha t}} \tag{3}$$

The ratio between temperature difference, θ_z/θ_s, is 0.01 when z^* is 1.58. The time corresponding to z^* is 30.4 seconds when depth z=5 mm. Although conduction also takes place from the other side of the wedge, 5-mm thickness of Teflon is enough to assure a semi-infinite solid approximation for the test that only lasts 4 to 5 seconds. For an accurate measurement by infrared thermography, all surfaces of the test plate were coated by a black paint with an emissivity of 0.97. The change in a thickness due to the applied paint was negligible and did not have a significant effect on the conduction in the test plate.

The surface temperature of the test plate was measured by an infrared camera (Jenoptik, Varioscan3011-ST) during the wind tunnel run. The camera was equipped with an uncooled microbolometer sensor with a resolution of 384 x 288 pixels and a maximum frame rate of 60 Hz. It measured a long-wave infrared signal (7.5-14 μm), and measurement temperature range was -40 to 500˚C. Resolution of temperature measurement at room temperature is at least 0.08 K and ideally around 0.05 K, according to the manufacturer.

2.3. Reduction of heat flux and heat transfer coefficient

A convective heat flux on the surface is considered to be the same as a conductive heat flux into a solid. As the surface temperature is below room temperature, cooled from 295 K to 275 K during a measurement, the radiative heat flux at the surface can be neglected. A common practice for determination of the convective heat flux is considering the heat flux balance on the model surface locally in one-dimension. Given the low heat conductivity material such as Teflon, lateral conduction is negligible and semi-infinite solid approximation is valid during the testing time. At any point of the surface, the heat flux is

$$\dot{q}_{cond} = \dot{q}_{conv} = h(T_{aw} - T_s) \tag{4}$$

Where $\dot{q}_{cond}$ is conductive heat flux, $\dot{q}_{conv}$ denotes convective heat flux, h is convective heat transfer coefficient, T_{aw} and T_s are adiabatic wall temperature and surface temperature, respectively.

In addition, a change of a solid temperature due to the surface heat flux is governed by a three-dimensional energy conservation equation as described below:

$$\frac{\partial^2 T}{\partial x^2} + \frac{\partial^2 T}{\partial y^2} + \frac{\partial^2 T}{\partial z^2} = \frac{1}{\alpha}\frac{\partial T}{\partial t} \tag{5}$$

Assuming a one-dimensional heat transfer in an in-depth direction from the surface, while neglecting a lateral conduction, following equations are valid:

$$\frac{\partial^2 T}{\partial x^2} \ll \frac{1}{\alpha}\frac{\partial T}{\partial t} \quad and \quad \frac{\partial^2 T}{\partial y^2} \ll \frac{1}{\alpha}\frac{\partial T}{\partial t} \tag{6}$$

$$\frac{\partial^2 T}{\partial z^2} = \frac{1}{\alpha}\frac{\partial T}{\partial t} \tag{7}$$

When the semi-infinite solid approximation is valid, and the conduction occurs only in the in-depth direction, the conductive heat flux into a solid at a time t can be deduced from a time history of the surface temperature.

$$\dot{q}_{cond}(t) = \sqrt{\frac{\rho c k}{\pi}}\left[\left\{\frac{T_s(t) - T_s(0)}{\sqrt{t}}\right\} + \frac{1}{2}\int_0^t \frac{T_s(t) - T_s(\tau)}{(t-\tau)^{3/2}} d\tau\right] \tag{8}$$

The integral term in Eq. (8) can be expressed as summation forms by assuming a linear variation of the temperature between each measurement separated by the time step, Δt. Then, the conductive heat flux at a time t_n, n time steps after initial time t_0, is as follows [29, 30]:

$$\dot{q}_{cond}(t_n) = \sqrt{\frac{\rho c k}{\pi}} \left\{ \frac{T_s(t_n) - T_s(t_0)}{\sqrt{t_n}} + \sum_{i=1}^{n-1} \left[\frac{T_s(t_n) - T_s(t_i)}{(t_n - t_i)^{\frac{1}{2}}} - \frac{T_s(t_n) - T_s(t_{i-1})}{(t_n - t_{i-1})^{\frac{1}{2}}} + 2\frac{T_s(t_i) - T_s(t_{i-1})}{(t_n - t_i)^{1/2} + (t_n - t_{i-1})^{1/2}} \right] + \frac{T_s(t_n) - T_s(t_{n-1})}{\sqrt{\Delta t}} \right\} \quad (9)$$

However, the above equation, based on a one-dimensional assumption, is not valid in the region around the injection hole. As the low temperature sonic jet flows inside the hole and cools the inner hole surface, the conduction in this region occurs in a three-dimensional manner. This leads to an additional temperature drop near the injection hole, depicted as the black line in Fig. 5. Because heat flux is deduced by the temperature drop from an initial temperature, a measured heat flux would be higher compared to an actual heat flux on the surface, shown by comparison between the red line and the blue line in Fig. 5. Therefore, care should be taken in deducing heat flux near the injection hole.

In this research, the three-dimensional transient energy equation of Eq. (5) is solved based on the finite volume method to accurately measure the heat transfer near the injection hole. The overall deduction procedure of a heat flux is shown in Fig. 6. First, measured IR images are interpolated into a computational surface grid by a least square interpolation for each time step. The interpolated surface temperatures are used as Dirichlet boundary conditions at each time for the finite volume calculation. A boundary condition for the surface inside the hole is calculated by CFD simulation of the flow with a Mach number of 1.0 and a total pressure corresponding to each momentum ratio. For the CFD of the flow inside the hole, SST k-ω turbulence model was used in two-dimensional domain. The structured grids having 0.1 million elements were selected based on the grid independence test, and the height of the first cell near the wall was set to get wall y+ less than 1. The calculated heat transfer coefficient inside the hole, h_h, is assumed to be constant in time and h_h and $T_{aw,h}/T_0$ deduced from the CFD simulation are applied as a mixed boundary condition. In addition, all other walls including lower side of the Teflon block is assumed to be adiabatic. With these boundary conditions, a transient conduction in the Teflon block of the test plate with a thickness of 5 mm is solved with 1.1 million computational cells and a time step of 0.01667 sec (as surface temperature is taken

with 60 Hz). All spatial and temporal gradients are discretized with 2nd-order implicit scheme and the heat flux on the surface, $\dot{q}_{conv}(t)$, at each time step is deduced.

After the heat flux on the surface is obtained, Eq. (4) can be used to obtain the heat transfer coefficient, h. However, the effect of a temperature drop in the wind tunnel should be considered in the process. As the total temperature of the flow drops due to the Joule–Thomson effect at pressure tanks and valves, the reference temperature for the heat transfer, T_{aw}, changes with time. In order to eliminate the effect of a temperature drop, a ratio of the adiabatic wall temperature and the total temperature is defined per the equation below:

$$\frac{T_{aw}(t)}{T_0(t)} = \frac{1 + r\frac{\gamma - 1}{2}Ma^2{}_\infty}{1 + \frac{\gamma - 1}{2}Ma^2{}_\infty} \tag{10}$$

As shown in Eq. (10), the value of $T_{aw}(t)/T_0(t)$ does not change with total temperature when the flow conditions are constant, thus Mach number, Ma_∞, and recovery factor, r, at a certain location do not change. This ratio is applied to Eq. (4) by dividing both side of the equation by the time-dependent total temperature of the flow, $T_0(t)$, as shown below:

$$\frac{\dot{q}_{conv}(t)}{T_0(t)} = h\left(\frac{T_{aw}(t)}{T_0(t)} - \frac{T_s(t)}{T_0(t)}\right) \tag{11}$$

The equation shows that $\dot{q}_{conv}(t)/T_0(t)$ and $T_s(t)/T_0(t)$ are in a linear relationship with a slope, $-h$, when the flow condition is constant (means T_{aw}/T_0 and h are constant). Therefore, the time-dependent heat flux, $\dot{q}_{conv}(t)$, and the surface temperature, $T_s(t)$, at each location are both divided by the measured total temperature and least square fitted to obtain the heat transfer coefficient as a slope of the curve. The ratio T_{aw}/T_0 is also obtained from the curve fit results as a point of contact on the $T_s(t)/T_0(t)$ axis. By presenting both heat transfer coefficient and adiabatic wall temperature, heat transfer characteristics near the injection hole is further analyzed. Also, the results can be utilized to predict heat transfer from similar hot gas condition in conjunction with heat transfer coefficient, as proposed by Sourgen et al. [31].

2.4. Oil film visualization

In order to understand how the flow affects surface heat transfer, oil film is used to visualize flow structure on the surface. Carbon particles are mixed with a silicon oil to control the viscosity of the oil and to enhance a visibility of the surface streamline. The mixture is applied to the surface of the test plate and distributions of the film are taken after a wind tunnel run with camera.

3. Results

3.1. Basic characteristics of heat transfer

Figure 7 shows normalized heat flux distributions around the injection hole with J = 1.018 at 0.5 sec and 2.5 sec after the start of the wind tunnel. The heat flux at each time step is normalized by laterally averaged values of the undisturbed upstream region at X/D = -6.0, which are 9955.5 and 7167.7 W/m^2, respectively. As shown in Fig. 7 (a), heat flux from the crossflow is initially decreased when the flow is separated at the periphery of the separation region around X/D = -2.0. After the separation, heat flux is rapidly increased to twice that of the undisturbed freestream due to the turbulent mixing of vortices. The heat flux is low at the separation region behind the injection jet, which splits into two smaller regions later due to the reattachment of the jet at the downstream. The characteristics of the heat transfer remain the same at 2.5 sec after the start of the wind tunnel, although the ratio of the heat flux in the jet interaction region is decreased as the temperature difference between the test plate and the flow decreases.

The effect of the hole conduction can be observed by comparing the upper and the lower side of Fig. 7. The surface temperature in the immediate vicinity of the injection hole drops faster than the other region as this area is cooled by both the freestream and the jet inside the hole. As a result, the heat flux in this area is reduced as shown in the lower half of Fig. 7 (a). However, cooling inside the injection hole could not be considered properly under the one-dimensional assumption, leading to an over prediction of the heat flux as shown in the upper half of Fig. 7 (a). The difference in the heat flux according to the deduction method is much clear in Fig. 7 (b) as the effect of the hole conduction propagates with time. Also, the trail of the separation region behind the jet is clearer when the three-dimensional conduction is considered in the deduction process of the heat flux. In summary, the accuracy of the heat flux measurement is evidently increased when the three-dimensional conduction

is taken account, especially near the injection hole. Therefore, further analysis of the heat transfer is carried out by considering the three-dimensional conduction.

As discussed in §2.3, a heat transfer coefficient and an adiabatic wall temperature at $J = 1.018$ are deduced from time histories of the heat flux and the surface temperature, which is depicted with oil film visualization in Fig. 8. The separation of the crossflow and resulting drop in shear stress appear as a dark streak of carbon particles at the upstream region in the oil film visualization. Another streak is formed between the separation region and the recirculation region, because the particles in the other area are carried away by the separation and recirculation vortices. Two streaks of the particle become darker and wider in spanwise direction from the centerline ($Y/D = 0.0$) as the strength of the separation and the recirculation vortices decreases. Also, a weak streak of the particle at the downstream region of the hole shows a separation and a reattachment of the jet. This flow phenomena could be better understood through more detailed oil film visualization results [32-34].

The heat transfer coefficient is greatly affected by the interaction of the jet and crossflow. As shown in the lower half of Fig. 8 (a), the heat transfer coefficient is initially decreased at the periphery of the separation region, rapidly increased afterwards through the separation and the recirculation region due to a turbulent mixing of the vortices. The heat transfer augmentation by the separation vortex and the recirculation vortex are not separable at the frontal area of the hole. However, it becomes distinguishable away from the centerline as the distance between two vortices increases. The maximum heat transfer at the immediate vicinity of the hole is thought to be caused by an unsteadiness of the jet mixing layer as suggested by S. Kawai et al. [17]. As described in their work, a flow between the bow shock and the barrel shock of the erupting jet vibrates significantly, which can cause a high heat transfer near the hole. This region also appears slightly darker than the other area of the recirculation region in the oil film visualization. From this observation, it can be inferred that the shear stress in this area could not act in a single direction and wash away the oil on the surface due to the oscillation of the flow. In the downstream region of the hole, an area with a low heat transfer coefficient exists at the jet separation region, and a modest increase in the heat transfer is observed at the reattachment point between the jet separation regions.

The location of the major shock wave can be deduced from the distribution of adiabatic wall temperature, as shown in Fig. 8 (b). As the crossflow separates from the surface, the adiabatic wall temperature rises at the periphery of the separation region due to the shock wave. At the downstream of the separation shock (Lambda shock) wave, the total temperature around the injection hole is fully recovered to that of the crossflow, indicates the location of the bow shock. On the other hand, the adiabatic wall temperature in the jet separation region behind the hole is lower than that of the freestream due to a low density in this region. Noise inside the jet separation region is caused by a low heat transfer coefficient of this area that resulted in a vibration of a point of contact in the curve-fitting process.

Figure 9 (a) shows the quantitative variation of the heat transfer coefficient in a streamwise direction. The heat transfer coefficient of the undisturbed upstream region is gradually decreased as the boundary layer develops. In front of the separation shock, the heat transfer coefficient is around 500 $W/m^2 \cdot K$. This value is consistent with the experimental value of Yu et al. [28] measured in the same wind tunnel and the experimental correlation for turbulent boundary layer suggested by R. Monaghan [35]. As the boundary layer separates and strong vortices develop at the separation region, the heat transfer is significantly increased at the downstream of the separation line. The maximum of the heat transfer, about 7 times that of the freestream, occurs in front of the injection hole on the centerline shown as the black line in Fig. 9 (a). The heat transfer behind the hole is low due to the low-pressure recirculation zone. In addition, it increases afterward when the jet reattaches to the surface. The augmentation of the heat transfer by the vortices is gradually decreased as vortices move away from the centerline at positions with higher *Y/D*. Also, the effect of each vortex on the heat transfer becomes distinguishable at higher *Y/D* as previously mentioned in Fig. 8.

As mentioned, the locations of shock waves can be speculated from the distribution of the adiabatic wall temperature, as shown in Fig. 9 (b). As shown as the black line, first increase in the adiabatic wall temperature is caused by the separation shock at *X/D* around -2.0 at the centerline. The temperature rises again at *X/D* around -1.0, indicating the location of the bow shock. At a position with higher *Y/D*, the locations of the 1st and 2nd peak move toward the downstream. In addition, the position change of the 2nd peak is larger than that of the 1st peak. This indicates that the width of the bow shock

is much narrower than that of the separation shock (Lambda shock). The increase of the temperature due to the shock wave become smaller at higher *Y/D* and this change is more pronounced at the bow shock. Also, it is notable that the positions of the separation shock and the bow shock are distinguishable in the adiabatic wall temperature, while it is neither in the heat flux nor the heat transfer coefficient at the centerline.

3.2. Effect of momentum ratio

As the momentum of the jet increases, jet acts as a larger and stronger obstacle to the crossflow. The barrel shock, bow shock and lambda shock develops on a larger scale [36], and the boundary layer separation is moved upstream. The size of recirculation region induced by the interaction between the bow shock and upstream boundary layer of jet also becomes larger [37].

In terms of heat transfer, figure 10 shows the distributions of the heat transfer coefficient and normalized adiabatic wall temperature with three different momentum ratios. As the momentum ratio increases, considerable phenomena regarding surface heat transfer coefficient have been observed. Firstly, the area affected by jet and crossflow interaction become wider in a spanwise direction, which is related to both the separation and recirculation of crossflow. Secondly, there is a notable change in the heat transfer at the trail of recirculation vortex as it significantly extends to the downstream region in a case with a higher momentum ratio. Thirdly, the jet separation region behind the hole, where it shows low heat transfer coefficient, also extends farther downstream because the flow separation behind the hole become more severe as the momentum of the jet increases. Finally, for all momentum ratios, the maximum heat transfer is caused by the oscillatory behavior in the vicinity of the hole and the augmentation of the heat transfer by the oscillation does not show a significant change according to the momentum ratio either in terms of area or magnitude.

The magnitude of the temperature recovery by the upstream shock waves is similar for all three cases, as shown in the lower half of Fig. 10. The location and the strength of the bow shock does not vary significantly, while the separation shock (Lambda shock) becomes wider in a spanwise direction at high momentum ratio. At the downstream of the injection hole, the temperature recovery of the $J = 0.510$ case shows a different pattern compared to those of the other cases. It seems that the effect

of the reattachment of the jet and a reflected shock wave is weak, as the jet separation region downstream of the hole is small in the $J = 0.510$ case. Therefore, the temperature at the downstream is recovered quickly in the $J = 0.510$ case, compared to the other cases. On the other hand, the effect of the reattachment of the jet and the shock reflection from the reattachment point is clearly visible in $J = 1.018$ and $J = 1.477$ cases, such as the momentum ratio of the jet to the crossflow, $J \geq 1$.

For a qualitative analysis, streamwise distributions of the heat transfer coefficient and the adiabatic wall temperature with different momentum ratios at several *Y/D* positions are shown in Figs. 11 and 12. As the momentum ratio increases, the upstream separation is provoked earlier on the centerline, as shown in Fig. 11 (a). However, the maximum of the heat transfer coefficient is not changed significantly. The magnitude of the heat transfer at the reattachment point downstream of the hole also does not show significant change, while the location of the reattachment point moves in a downstream direction with an increasing momentum ratio. At the position away from the centerline, the change of the upstream separation point become more distinctive as shown in Fig. 11 (b) and (c). The initial increase of the heat transfer at the separation point seems to be similar in magnitude. However, the magnitude of the 2nd peak is strongly affected by the recirculation vortex, showing a higher value, especially in the $J = 1.477$ case at $Y/D = 2.0$.

The location of the separation shock moves in the upstream direction as the momentum ratio increases, which can be inferred from the distribution of the adiabatic wall temperature in Fig. 12. However, the location of the bow shock does not show a noticeable variation at the centerline with the momentum ratio. This can be confirmed by the similar slope of the temperature after the separation shock towards the injection hole at the centerline. The location and magnitude of the bow shock is also similar at a $Y/D = 1.0$ position as the 2nd peak is located near *X/D* around 0.0. On the contrary, the recovery of the temperature at the downstream of the hole occurs earlier in the $J = 0.51$ case, showing a rapid increase of the temperature behind the hole at the centerline. A drop of the adiabatic wall temperature observed in the blue line in Fig. 12 (b) is attributed to the separation region behind the bow shock. A rapid increase after that point is caused by a reflected shock from the reattachment point of the jet.

Finally, a change in an interaction area and an augmentation of heat transfer coefficient on an interaction and a near-hole area with respect to the momentum ratio are shown in Fig. 13. For this purpose, an augmentation of heat transfer coefficient is defined as follows.

$$h_{aug} \equiv \frac{\sum_{area} hA_{pixel}}{\sum_{area} h_{\infty} A_{pixel}}$$

In the upper part, the heat transfer coefficient on an interaction area or near-hole area is multiplied by a pixel area and summed over a corresponding area. Then, it is divided by a sum of the heat transfer coefficient on an undisturbed crossflow times a pixel area. Therefore, it represents the amount of augmentation in the heat transfer on an area compared to the original crossflow condition. In addition, the interaction area is defined as the summation of the streamwise pixel strip after the crossflow separation in lateral direction. The crossflow separation is recognized as a point with continuous increase of the heat transfer coefficient in three streamwise pixels and a heat transfer coefficient larger than 110% of the freestream value. A near-hole region is defined as a point from which the distance to the hole center is lower than the diameter of the injection hole.

As shown in Fig. 13, the interaction area shows linear increase with increasing jet momentum. It is increased by 37.3%, while the momentum ratio is increased from 0.51 to 1.477. In addition, augmentations of the heat transfer coefficient compared to the freestream on the jet interaction area and near-hole region are depicted as blue lines. Augmentation of the heat transfer coefficient on the interaction area is changed from 1.59 times the freestream to 1.92 times the freestream, corresponds to a 20.8% of change, when the momentum ratio changes from 0.51 to 1.477. A significant increase in the heat transfer is observed at the near-hole region where the heat transfer coefficient is increased 3.91 times the freestream value. It increases 28.6% in the J = 1.477 case, which corresponds to 5.03 times of the freestream value. Thus, this significant increase in the heat transfer should be considered for thermal design process. Especially, the heat transfer in the near-hole area should be considered properly, as it is augmented at least 390% compared to the freestream, even at the low momentum ratio.

4. Conclusions

In the present study, the heat transfer near the injection hole caused by an interaction between the supersonic crossflow with a Mach number of 3.0 and the sonic jet were investigated with three different momentum ratios (J = 0.510, 1.018, 1.477). Unlike previous studies, a three-dimensional conduction was considered in the deduction of heat transfer results to accurately analyze the behavior of the near-hole region. A comparison between deduction processes showed that a data reduction considering three-dimensional effect yielded better results at the near-hole region and captured flow features like separation more clearly.

The experimental results showed that the heat transfer was augmented by the separation and the recirculation vortex at the frontal area of the injection hole, while a separation and a reattachment of the jet governed the heat transfer downstream of the hole. The recirculation vortex showed a higher influence on the heat transfer, especially when coupled with an oscillatory behavior of the flow structure at the near-hole region. Maximum heat transfer coefficient near the hole was found to be 3800 W/m^2K, while the freestream value before the separation was around 470 W/m^2K.

When the momentum ratio was increased, the separation shock became wider and moved to upstream direction. The change in the position of the shock was more evident in the separation shock, while the location of the bow shock did not show a noticeable change. The influence of the recirculation vortex on the heat transfer was extended both in a spanwise direction and to a downstream area at a higher momentum ratio. Due to a wider separation shock, the jet interaction area was increased linearly with momentum ratio. The resulting augmentation of heat transfer in the jet interaction area compared to the freestream value was found to be changed from 159% to 192%. Furthermore, the augmentation of heat transfer at the near-hole area was at least 390% at the low momentum ratio and could increase up to 503% with J = 1.477. Therefore, the augmentation of heat transfer near the injection hole should be considered properly. When thermal designing a system with similar flow physics, the type and thickness of composite material [38] should be chosen considering the augmentation of heat transfer near the hole. Appling titanium or abrasives locally to the wall near the injection hole could be a way to protect the thermal components.

References

[1] J. E. Broadwell, “Analysis of the fluid mechanics of secondary injection for thrust vector control,” AIAA Journal, vol. 1, no. 5, pp. 1067–1075, May 1963.

[2] M. Shandor, A. R. Stone, and R. E. Walker, “Secondary gas injection in a conical rocket nozzle,” AIAA Journal, vol. 1, no. 2, pp. 334–338, Feb. 1963.

[3] I. Zeierman and Y. Manheimer-Timnat, “Full control of solid propellant rockets by secondary injection,” Journal of Spacecraft and Rockets, vol. 10, no. 3, pp. 161–162, Mar. 1973.

[4] C. Guo, Z. Wei, K. Xie, and N. Wang, “Thrust control by fluidic injection in solid rocket motors,” Journal of Propulsion and Power, vol. 33, no. 4, pp. 815–829, Jul. 2017.

[5] M. R. Gruber, A. S. Nejad, T. H. Chen, and J. C. Dutton, “Bow shock/jet interaction in compressible transverse injection flowfields,” AIAA Journal, vol. 34, no. 10, pp. 2191–2193, Oct. 1996.

[6] S. M. Torrez, J. F. Driscoll, M. Ihme, and M. L. Fotia, “Reduced-order modeling of turbulent reacting flows with application to ramjets and scramjets,” Journal of Propulsion and Power, vol. 27, no. 2, pp. 371–382, Mar. 2011.

[7] M. S. R. Chandra Murty, A. V. Bhandarkar, and D. Chakraborty, “Aerothermal exploration of reaction control jet in supersonic crossflow at high altitude,” Aerospace Science and Technology, vol. 50, pp. 266–271, Mar. 2016.

[8] A. Ben-Yakar, M. G. Mungal, and R. K. Hanson, “Time evolution and mixing characteristics of hydrogen and ethylene transverse jets in supersonic crossflows,” Physics of Fluids, vol. 18, no. 2, p. 026101, 2006.

[9] F. W. Spaid and E. ZUKOSKI, “Secondary injection of gases into a supersonic flow,” AIAA journal, vol. 2, no. 10, pp. 1689–1696, 1964.

[10] F. W. SPAID, “A study of secondary injection of gases into a supersonic flow,” Thesis (Dissertation (Ph.D.)), California Institute of Technology, 1964.

[11] J. G. Santiago and J. C. Dutton, “Velocity measurements of a jet injected into a supersonic crossflow,” Journal of Propulsion and Power, vol. 13, no. 2, pp. 264–273, Mar. 1997.

[12] L. Maddalena, T. L. Campioli, and J. A. Schetz, “Experimental and computational investigation of light-gas injectors in a Mach 4.0 crossflow,” Journal of Propulsion and Power, vol. 22, no. 5, pp. 1027–1038, Sep. 2006.

[13] G. J. McCann and R. D. W. Bowersox, “Experimental investigation of supersonic gaseous injection into a supersonic freestream,” AIAA Journal, vol. 34, no. 2, pp. 317–323, Feb. 1996.

[14] M. R. Gruber and L. P. Goss, “Surface pressure measurements in supersonic transverse injection flowfields,” Journal of Propulsion and Power, vol. 15, no. 5, pp. 633–641, Sep. 1999.

[15] Liu, Y., et al. "Turbulent boundary layer subjected to a sonic transverse jet in a supersonic flow." Aerospace Science and Technology 104 (2020): 106016.

[16] Erdem, Erinc, and Konstantinos Kontis. "Experimental investigation of sonic transverse jets in Mach 5 crossflow." Aerospace Science and Technology 110 (2021): 106419.

[17] S. Kawai and S. K. Lele, “Large-eddy simulation of jet mixing in supersonic crossflows,” AIAA Journal, vol. 48, no. 9, pp. 2063–2083, Sep. 2010.

[18] Zhao, Majie, et al. "Large eddy simulation of transverse single/double jet in supersonic crossflow." Aerospace Science and Technology 89 (2019): 31-45.

[19] Williams, Nehemiah J., Trevor M. Moeller, and Richard J. Thompson. "Numerical simulations of high frequency transverse pulsed jet injection into a supersonic crossflow." Aerospace Science and Technology 103 (2020): 105908.

[20] Sebastian, Robin, Thomas Lürkens, and Anne-Marie Schreyer. "Flow field around a spanwise-inclined jet in supersonic crossflow." Aerospace Science and Technology 106 (2020): 106209.

[21] Viti, Valerio, Reece Neel, and Joseph A. Schetz. "Detailed flow physics of the supersonic jet interaction flow field." Physics of fluids 21.4 (2009): 046101.

[22] Sun, Mingbo, and Zhiwei Hu. "Formation of surface trailing counter-rotating vortex pairs downstream of a sonic jet in a supersonic cross-flow." Journal of Fluid Mechanics 850 (2018): 551-583.

[23] Sun, Ming-Bo, and Z. W. Hu. "Generation of upper trailing counter-rotating vortices of a sonic jet in a supersonic crossflow." AIAA Journal 56.3 (2018): 1047-1059.

[24] W. Huang, “Transverse jet in supersonic crossflows,” Aerospace Science and Technology, vol. 50, pp. 183–195, Mar. 2016.

[25] G. T. Roberts, P. H. Schuricht, and N. R. Mudford, “Heating enhancement caused by a transverse control jet in hypersonic flow,” Shock Waves, vol. 8, no. 2, pp. 105–112, 1998.

[26] A. Guelhan, G. Schuette, and B. Stahl, “Experimental study on aerothermal heating caused by jet-hypersonic crossflow interaction,” Journal of Spacecraft and Rockets, vol. 45, no. 5, pp. 891–899, Sep. 2008.

[27] M. Taguchi, K. Mori, and Y. Nakamura, “Experimental study on aerodynamic heating induced by dual injections into hypersonic cross flow,” International Journal of Aerospace Engineering, 2017.

[28] M. S. Yu, J. Song, J. C. Bae, and H. H. Cho, “Heat transfer by shock-wave/boundary layer interaction on a flat surface with a mounted cylinder,” International Journal of Heat and Mass Transfer, vol. 55, no. 5–6, pp. 1764–1772, Feb. 2012.

[29] Alan Pope and Kenneth L. Goin. “High-speed wind tunnel testing.”, Wiley (1965)

[30] Henshall, B. D., and D. L. Schultz. "Some notes on the use of resistance thermometers for the measurement of heat transfer rates in shock tubes." (1959).

[31] F. Sourgen, T. Gauthier, F. Leopold, B. Sauerwein, and R. Meuer, “Substitution of hot-gas lateral jets by cold-gas jets in supersonic flows,” Journal of Spacecraft and Rockets, vol. 48, no. 1, pp. 81–92, Jan. 2011.

[32] Liang, Chang-hai, et al. "Shock wave structures in the wake of sonic transverse jet into a supersonic crossflow." Acta Astronautica 148 (2018): 12-21.

[33] Liang, Chang-hai, et al. "Experimental study of parallel injections with different distances into a supersonic crossflow." Acta Astronautica 168 (2020): 242-248.

[34] Liu, Yuan, et al. "Structures of near-wall wakes subjected to a sonic jet in a supersonic crossflow." Acta Astronautica 151 (2018): 886-892.

[35] R. J. Monaghan, M.A., “A Survey and Correlation of Data on Heat Transfer by Forced Convection at Supersonic Speed,” Ministry of Supply, Aeronautical Research Council, 1958.

[36] Génin, Franklin, and Suresh Menon. "Dynamics of sonic jet injection into supersonic crossflow." Journal of Turbulence 11 (2010): N4.

[37] Zhao, Majie, et al. "Study of sonic injection from circular injector into a supersonic cross-flow using large eddy simulation." International journal of hydrogen energy 41.39 (2016): 17657-17669.

[38] Choubey, Gautam, Lakka Suneetha, and K. M. Pandey. "Composite materials used in Scramjet-A Review." Materials Today: Proceedings 5.1 (2018): 1321-1326.

[39] L. H. Back, R. F. Cuffel, and P. F. Massier, “Flow phenomena and convective heat transfer in a conical supersonic nozzle.,” Journal of Spacecraft and Rockets, vol. 4, no. 8, pp. 1040–1047, Aug. 1967.

LIST OF TABLES

Table 1. Average flow conditions for each momentum ratio during data reduction

M_∞	T_0, K	p_0, bar	p,bar	p_{0si}, bar	resulting J	Re_∞
3	281.8	7.059	0.1922	1.670	1.477	1.24×10^6
3	281.8	7.059	0.1922	3.360	1.018	1.24×10^6
3	281.8	7.059	0.1922	4.863	0.510	1.24×10^6

LIST OF FIGURES

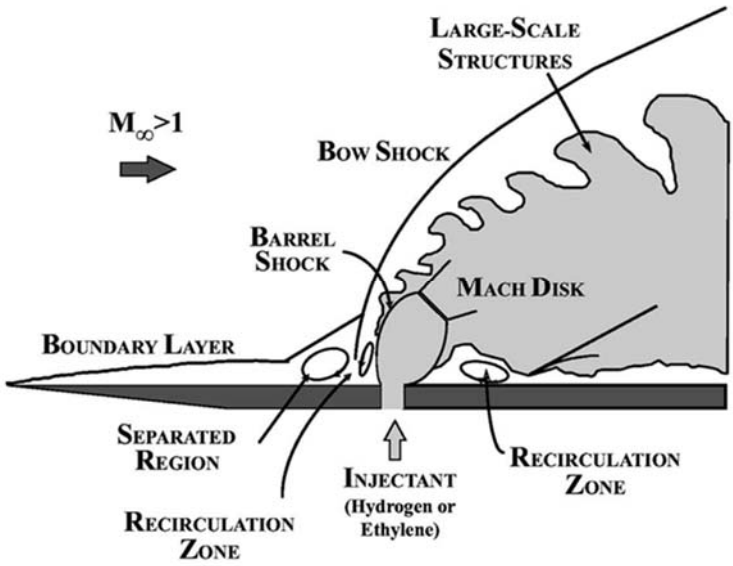

Figure 1. Schematics of typical flow structure with interaction between a sonic jet and supersonic crossflow [8]

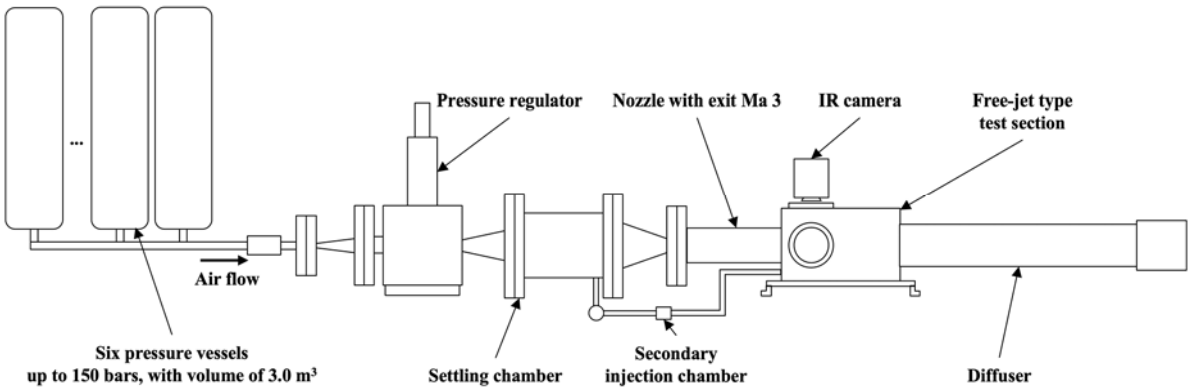

Figure 2. Schematic view of key components in the intermittent blowdown wind tunnel

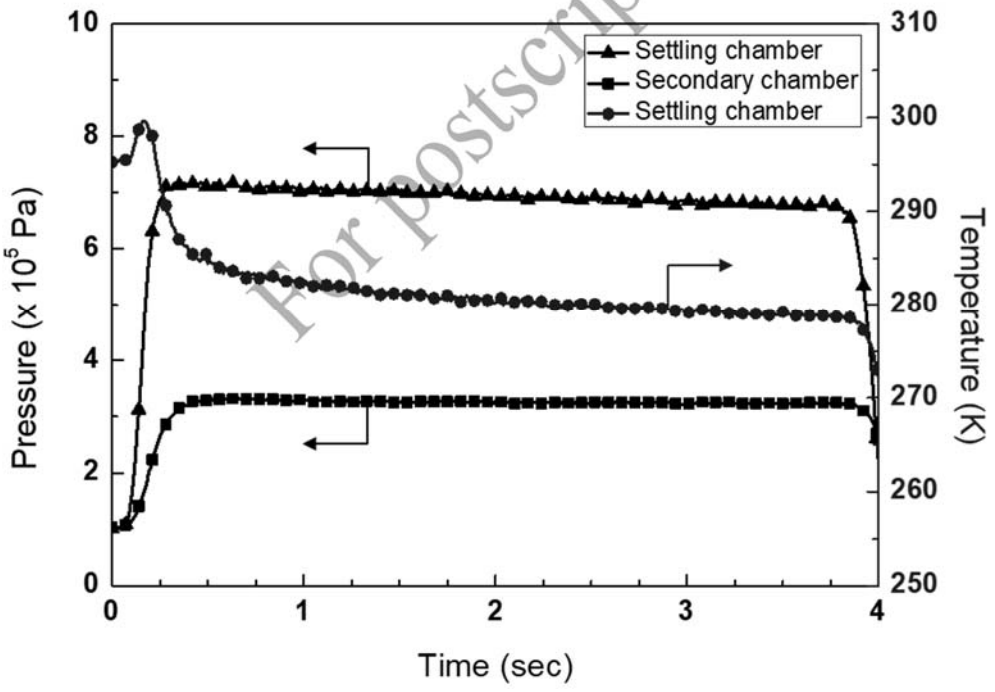

Figure 3. Typical flow conditions for 4-second run

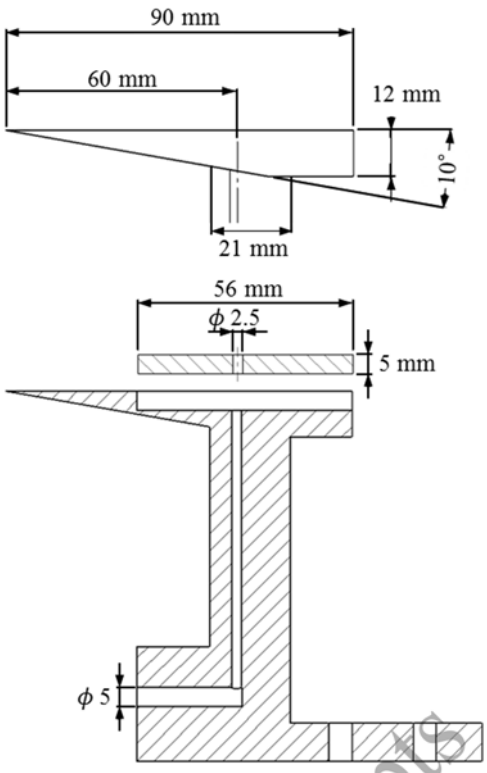

(a) Dimensions of the model

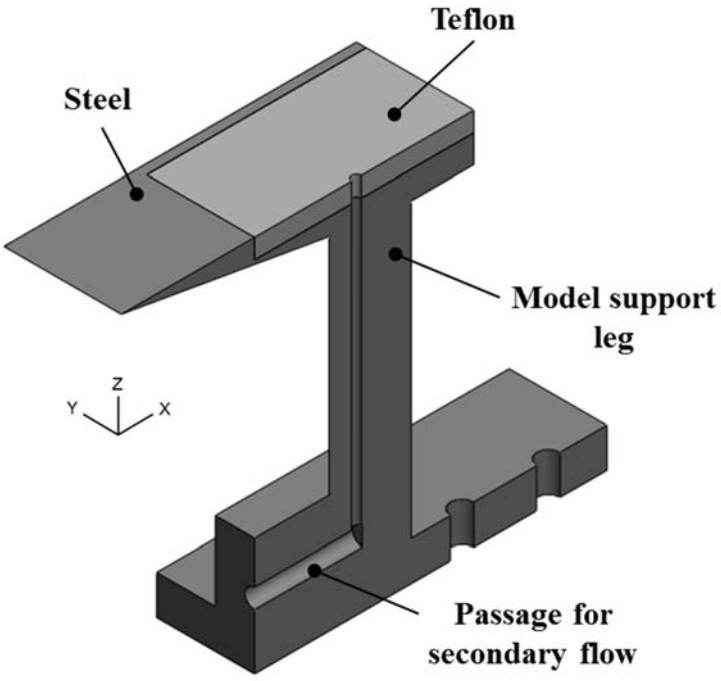

(b) Cross-sectional view of the model

Figure 4. Test plate with sonic jet injection composed of structural steel and Teflon insulation

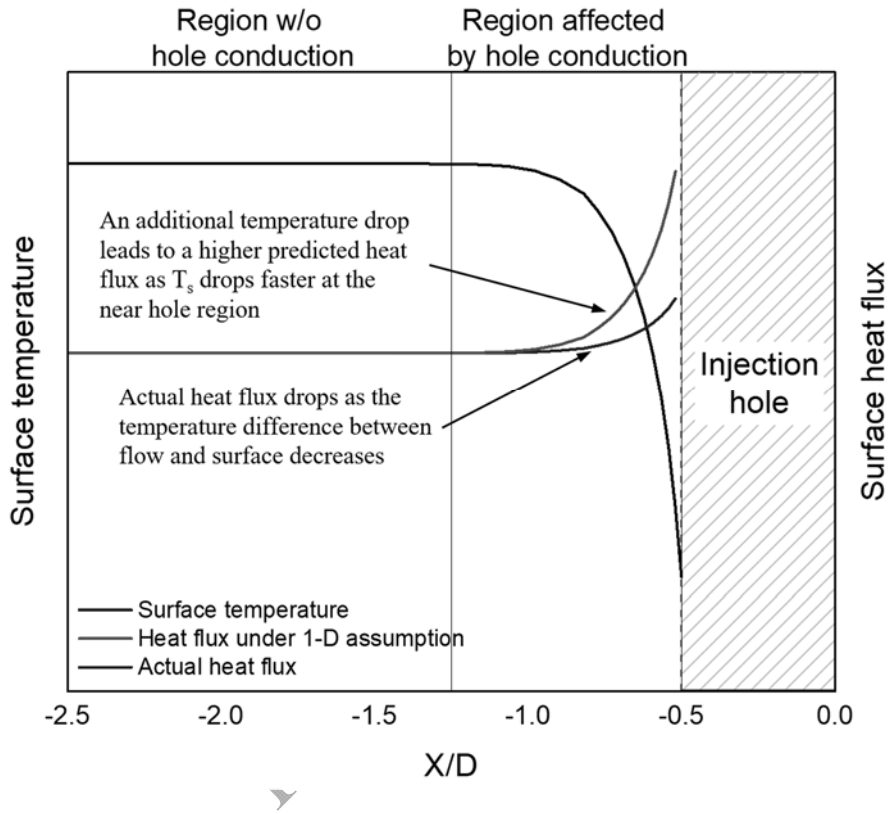

Figure 5. Possible effect of lateral conduction on measured/actual heat flux around injection hole

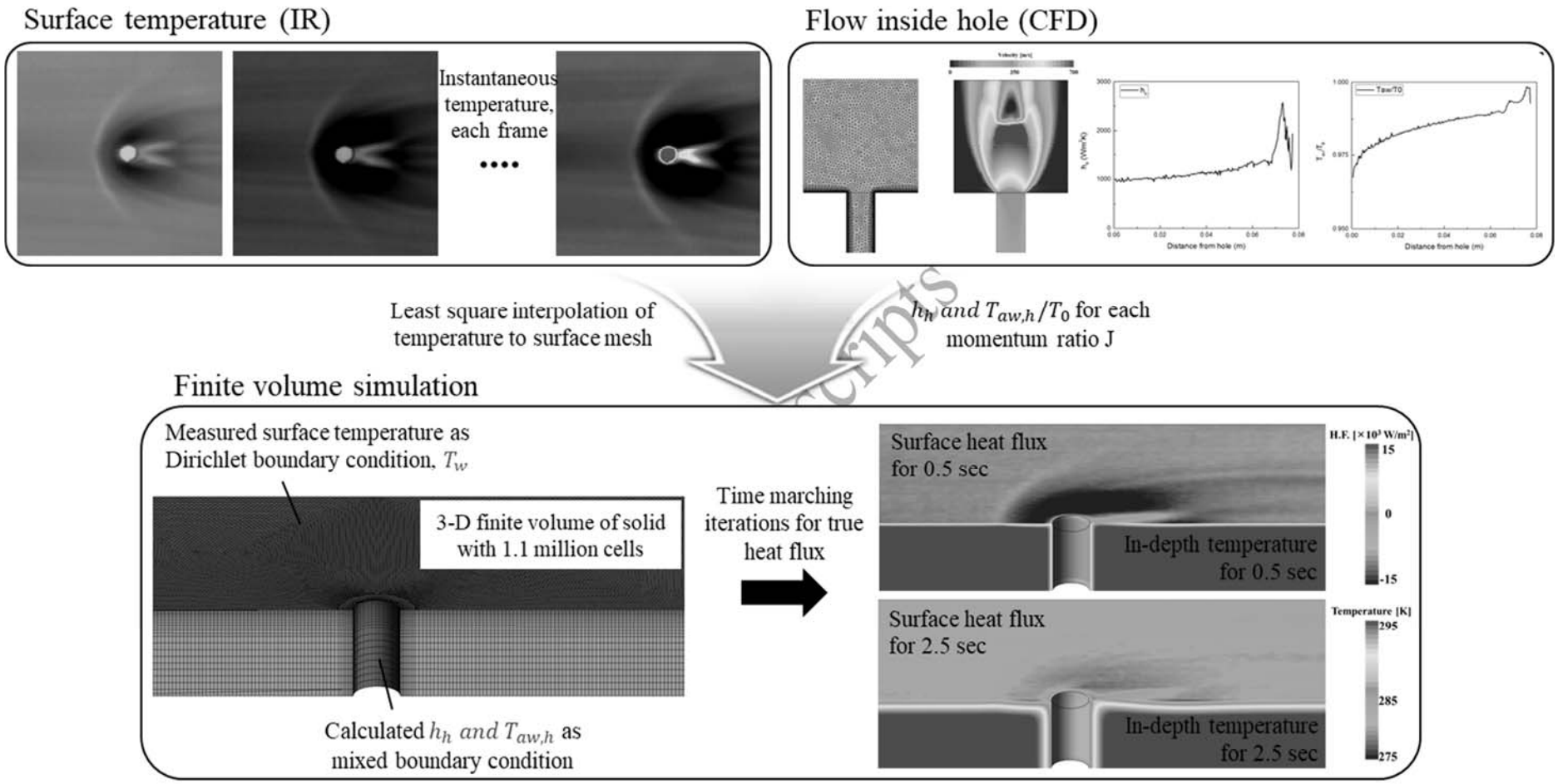

Figure 6. Procedures for heat flux deduction considering 3-D conduction near-hole

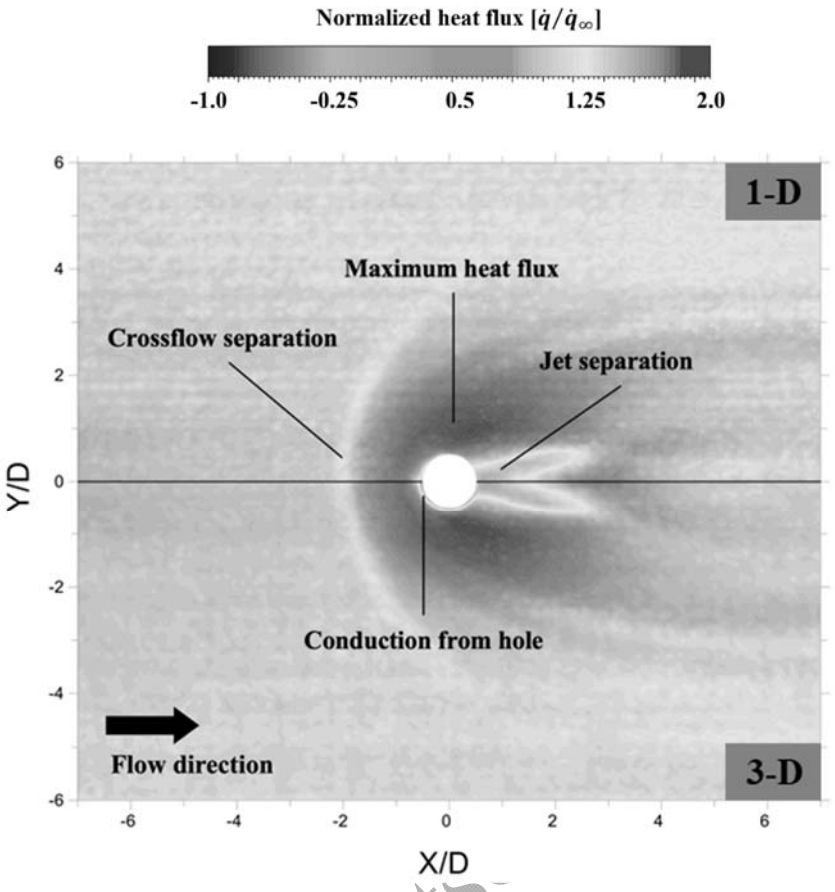

(a) 0.5 seconds after wind tunnel start

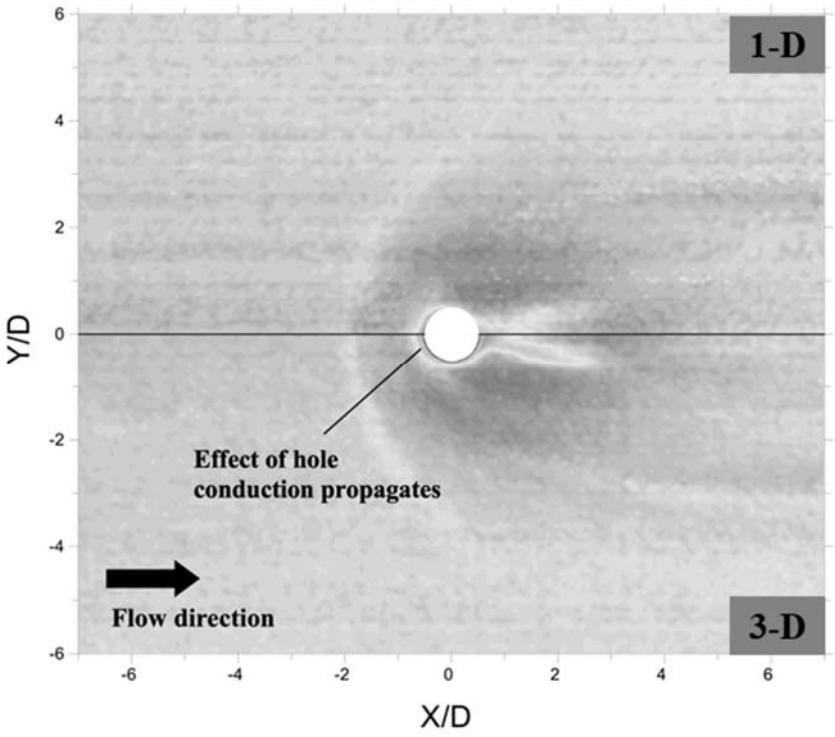

(b) 2.5 seconds after wind tunnel start

Figure 7. Normalized heat flux distribution of shock-affected region obtained by 1-D conduction (upper half) and 3-D conduction (lower half)

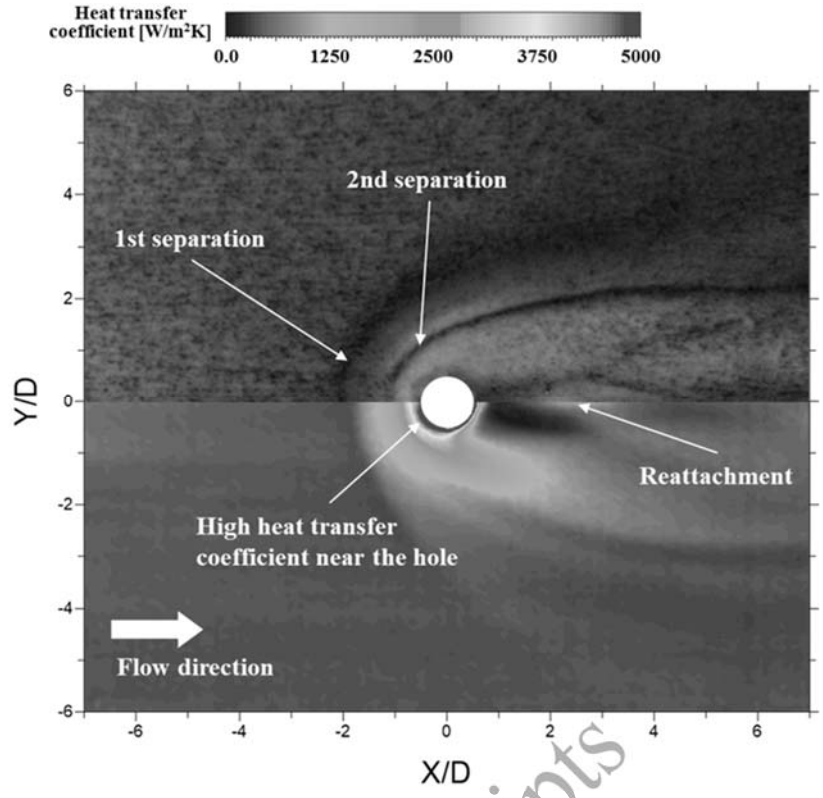

(a) Heat transfer coefficient distribution compared to oil film visualization

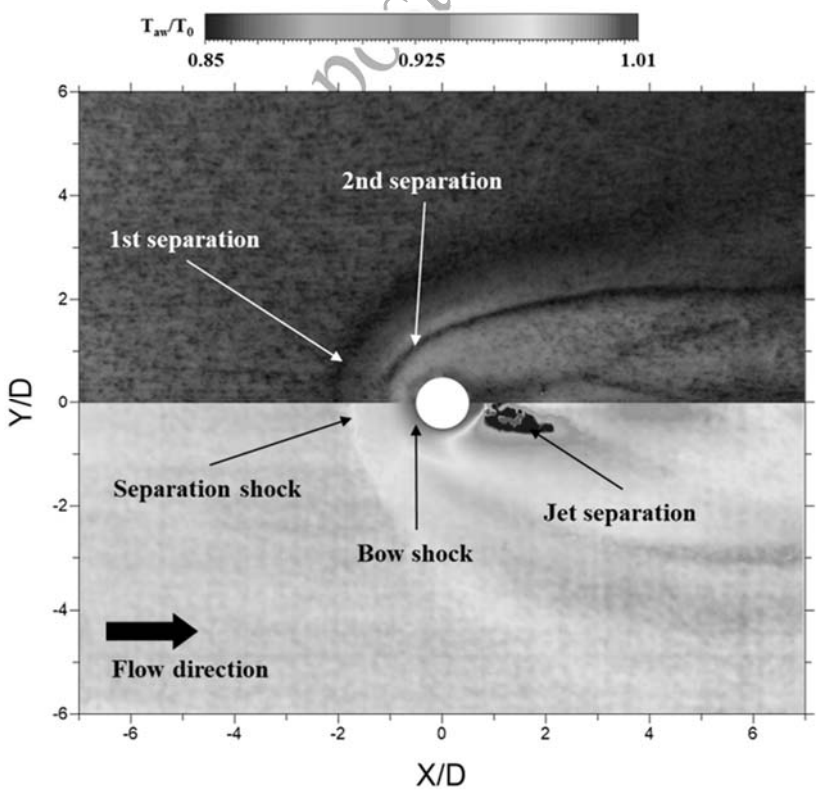

(b) Adiabatic wall temperature distribution compared to oil film visualization

Figure 8. Heat transfer characteristics and flow structure around injection hole at J = 1.018

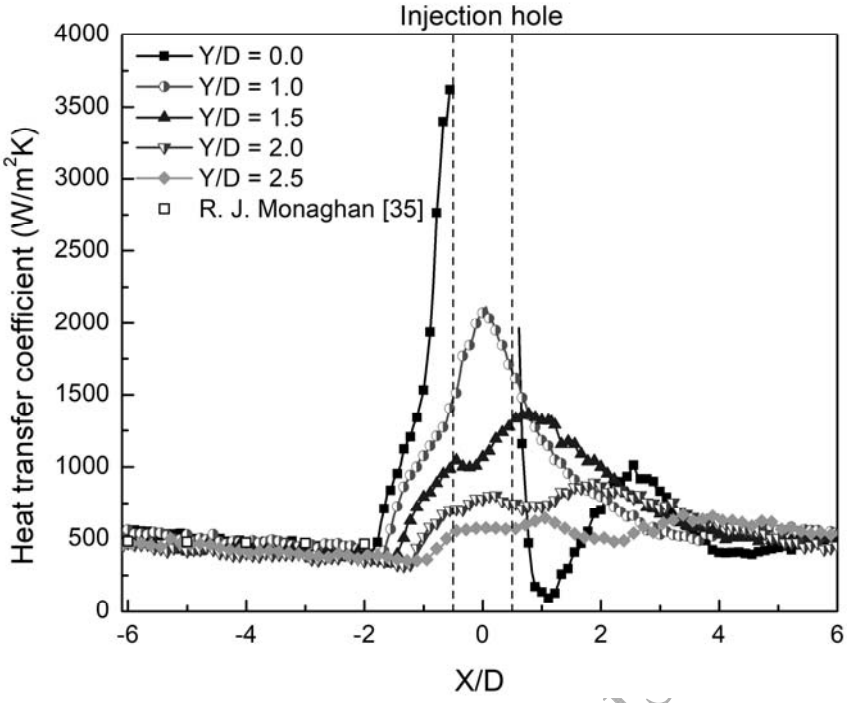

(a) Heat transfer coefficients in a streamwise direction for different Y/D

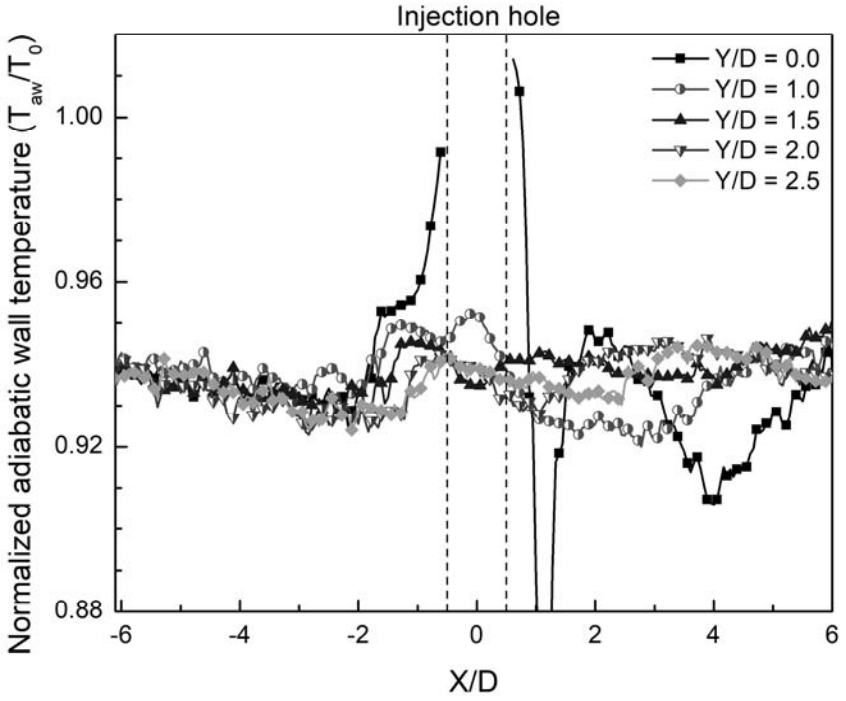

(b) Adiabatic wall temperatures in a streamwise direction for various Y/D

Figure 9. Distribution of heat transfer coefficients and adiabatic wall temperatures in streamwise direction

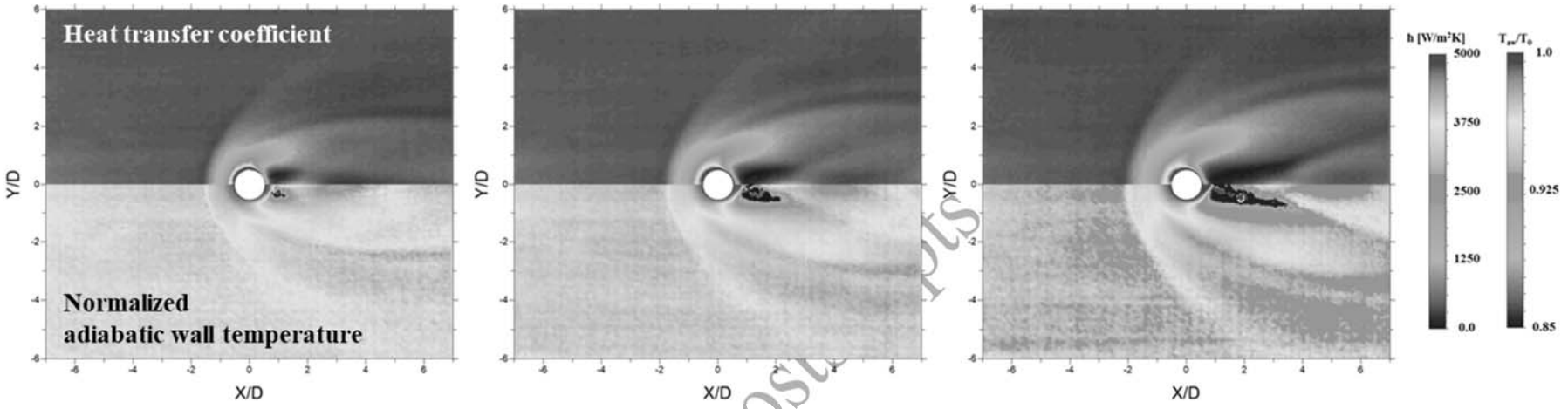

(a) $J = 0.510$ (b) $J = 1.018$ (c) $J = 1.447$

Figure 10. Contours of heat transfer coefficient and normalized adiabatic wall temperature

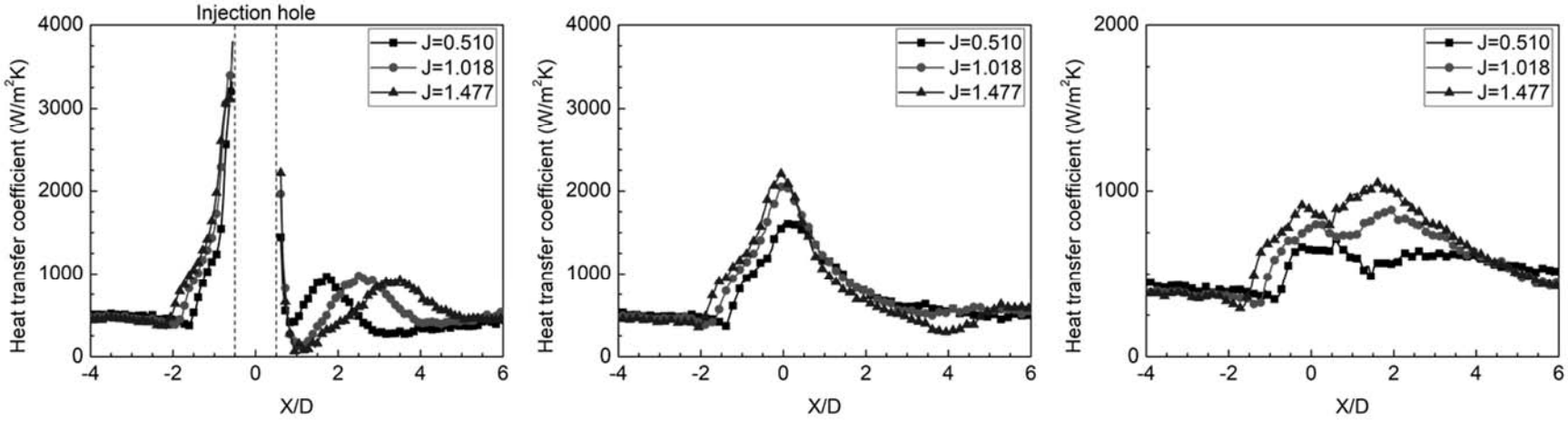

(a) Y/D = 0.0 (b) Y/D = 1.0 (c) Y/D = 2.0

Figure 11. Streamwise distribution of heat transfer coefficient with different momentum ratios

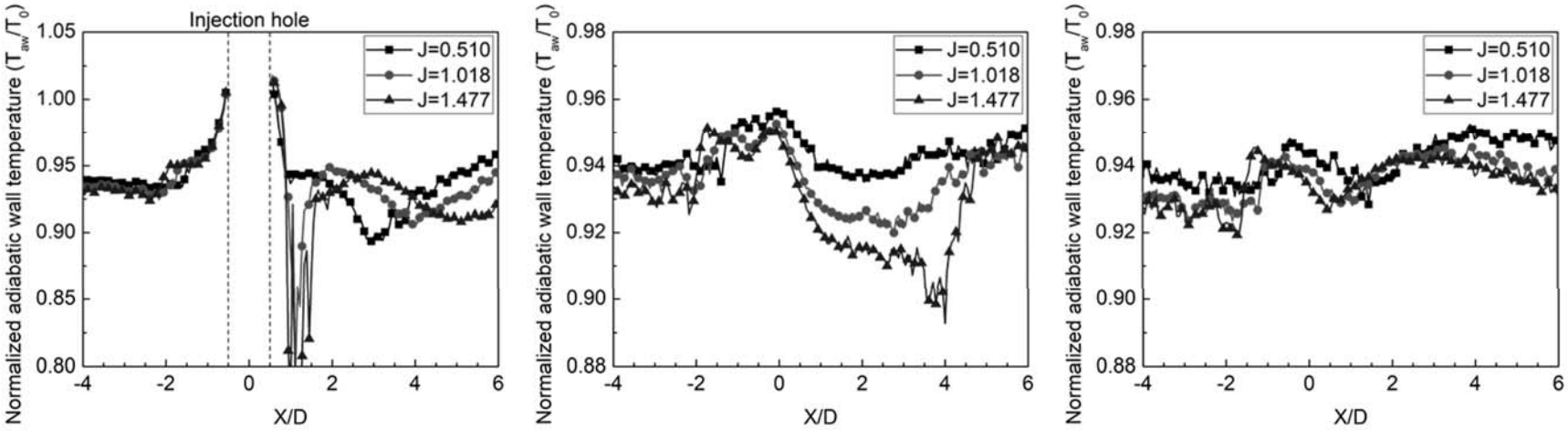

(a) Y/D = 0.0 (b) Y/D = 1.0 (c) Y/D = 2.0

Figure 12. Streamwise distribution of normalized adiabatic wall temperature with different momentum ratios

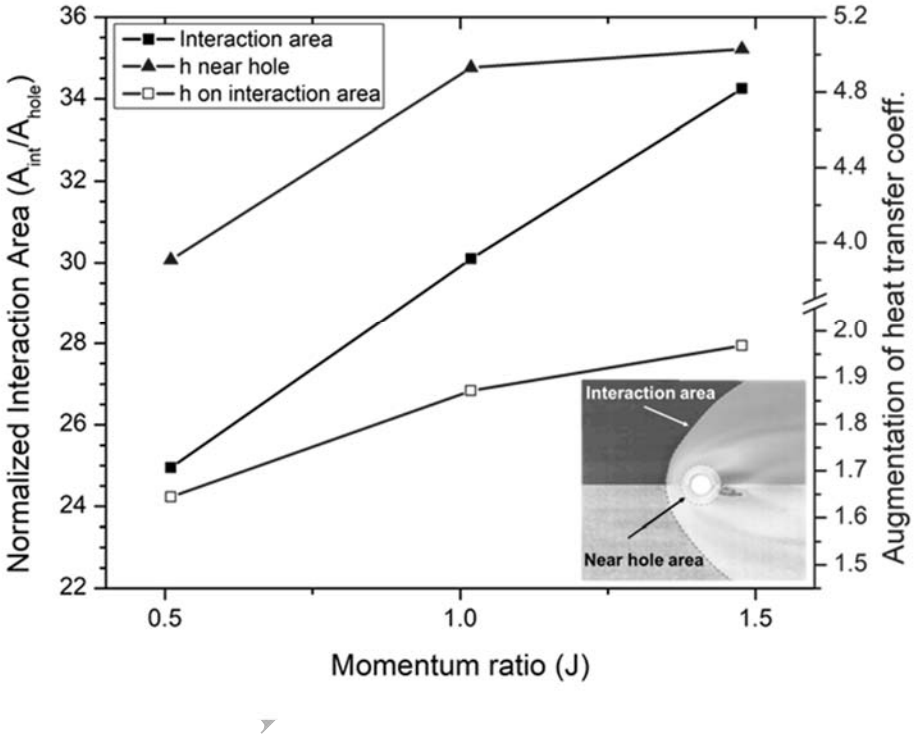

Figure 13. Change in interaction area and augmentation of heat transfer coefficient on surface for different momentum ratios

Response to the 1st reviewer's comments:

We appreciate the significant efforts that reviewers put into our paper to review. We will respond to the reviewer's comments and suggestions in detail in the following. According to the reviewer's opinion, we modified the manuscript with notification by highlighting and attached a full list of changes.

Comment (1)

The description of the numerics is rather poor. Which kind of mesh is used? Whic h is the order of accuracy? And the mesh independent verification should be added.

Answer to Comment (1)

As the reviewer pointed out, it is needed to describe numerical conditions in detail because the process of deriving the heat transfer results includes numerical methods.

The purpose of this research is to conjugate the experiment with the simulation of three-dimensional transient energy equation to accurately measure the heat transfer near the injection hole. In order to achieve this purpose, firstly, measured IR images are interpolated into a computational surface grid by a least square interpolation for each time step. The interpolated surface temperatures are used as Dirichlet boundary conditions at each time for the finite volume calculation.

Then, to acquire a boundary condition inside the hole for a secondary jet, CFD simulation is performed with a Mach number of 1.0 and a total pressure corresponding to each momentum ratio. The heat transfer coefficient inside the hole, h_h, is assumed to be constant in time and h_h and $T_{aw,h}/T_0$ deduced from the CFD simulation are applied as a mixed boundary condition. $T_{aw,h}$ is adiabatic wall temperature inside the hole, and T_0 is total temperature of jet. All other walls including lower side of the Teflon block is assumed to be adiabatic.

With these boundary conditions, a transient conduction in the Teflon block of the test plate with a thickness of 5 mm is solved with 1.1 million computational cells and a time step of 0.01667 sec (as surface temperature is taken with 60 Hz). All spatial and temporal gradients are discretized with 2nd-order implicit scheme and the heat flux on the surface, $\dot{q}_{conv}(t)$, at each time step is deduced.

To secure the boundary condition inside the hole, it is important to validate the simulated results with experimental results [39]. We compare the CFD analysis at the nozzle throat wall because the nozzle throat is the most severe change of thermo-fluidic behaviors and the Mach number is 1. Figure R1 shows that SST k-ω model provides most close results at the throat. In addition, we compare the mesh density near the wall based on the y+. As shown in Fig. R2, y+ sensitivity of SST k-ω shows

6.3 % of error up to y+ 30 at the throat. When wall y+ is 1, the heat flux at the nozzle neck most similar to the experimental result was obtained, and the error with the experimental value was 2.4 %. Therefore, in the two-dimensional domain, SST k-ω turbulence model was used for flow analysis inside the hole. Furthermore, we also tested the grid independence. The structured grids having 0.1 million elements were selected based on the grid independence test (Fig. R3), and the height of the first cell near the wall was set to get wall y+ less than 1.

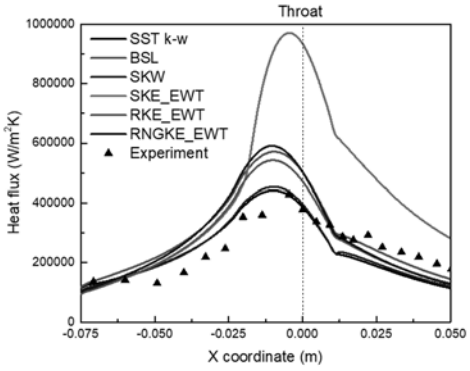

Figure R1 Nozzle wall heat flux according to turbulence model

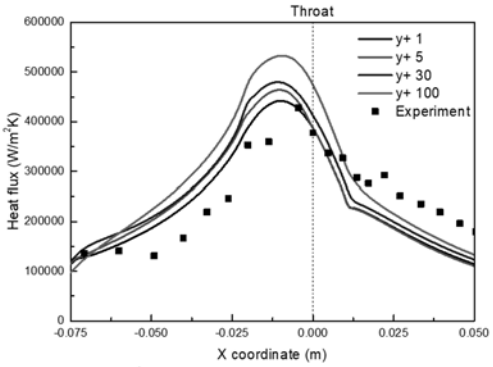

Figure R2 Nozzle wall heat flux according to wall Y+

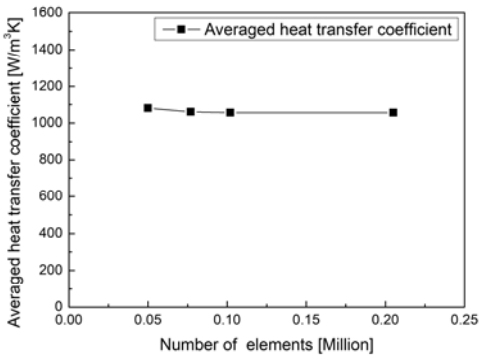

Figure R3 Heat transfer coefficient averaged over the hole length of the Teflon block

- **Added sentences in manuscript (page 9)**

For the CFD of the flow inside the hole, SST k-ω turbulence model was used in two-dimensional domain. The structured grids having 0.1 million elements were selected based on the grid independence test, and the height of the first cell near the wall was set to get wall y+ less than 1.

Comment (2)

Please explain the variables, such as Taw and qcond and qconv d in Eq 4. There plenty of variables lack their meanings.

Answer to Comment (2)

Thanks to the reviewer for pointing it out. In the last manuscript, there was not enough explanation about the variables. Considering the reviewer's comments, nomenclature has been added to the revised manuscript, and sentences in section 2.3 (the reduction of heat flux and heat transfer coefficient) has been revised to make it easier to understand.

- **Added sentences in manuscript (page 2)**

Nomenclature

J	= jet-to-freestream momentum ratio
ρ	= density
v	= velocity
γ	= specific heat ratio
p	= pressure
M	= Mach number
q_{cond}	= conductive heat flux
q_{conv}	= convective heat flux
h	= heat transfer coefficient
T	= Temperature
θ	= temperature difference
z	= depth
α	= thermal diffusivity
c	= specific heat capacity
k	= thermal conductivity
t	= time
D	= diameter of injection hole
h_{aug}	= augmentation of heat transfer coefficient
A_{pixel}	= area of a pixel

Subscripts

j	= jet exit property
∞	= freestream property
aw	= adiabatic wall condition
s	= surface property
0	= stagnation condition
h	= injection hole property

- **Revised sentences in manuscript (page 8)**

A convective heat flux on the surface is considered to be the same as a conductive heat flux into a solid. As the surface temperature is below room temperature, cooled from 295 K to 275 K during a measurement, the radiative heat flux at the surface can be neglected. A common practice for determination of the convective heat flux is considering the heat flux balance on the model surface locally in one-dimension. Given the low heat conductivity material such as Teflon, lateral conduction is negligible and semi-infinite solid approximation is valid during the testing time. At any point of the surface, the heat flux is

$$\dot{q}_{cond} = \dot{q}_{conv} = h(T_{aw} - T_s) \quad (4)$$

Where q_{cond} is conductive heat flux, q_{conv} denotes convective heat flux, h is convective heat transfer coefficient, T_{aw} and T_s are adiabatic wall temperature and surface temperature, respectively.

In addition, a change of a solid temperature due to the surface heat flux is governed by a three-dimensional energy conservation equation as described below:

$$\frac{\partial^2 T}{\partial x^2}+\frac{\partial^2 T}{\partial y^2}+\frac{\partial^2 T}{\partial z^2}=\frac{1}{\alpha}\frac{\partial T}{\partial t} \tag{5}$$

Assuming a one-dimensional heat transfer in an in-depth direction from the surface, while neglecting a lateral conduction, following equations are valid:

$$\frac{\partial^2 T}{\partial x^2} \ll \frac{1}{\alpha}\frac{\partial T}{\partial t} \quad and \quad \frac{\partial^2 T}{\partial y^2} \ll \frac{1}{\alpha}\frac{\partial T}{\partial t} \tag{6}$$

$$\frac{\partial^2 T}{\partial z^2}=\frac{1}{\alpha}\frac{\partial T}{\partial t} \tag{7}$$

When the semi-infinite solid approximation is valid, and the conduction occurs only in the in-depth direction, the conductive heat flux into a solid at a time t can be deduced from a time history of the surface temperature.

$$\dot{q}_{cond}(t)=\sqrt{\frac{\rho c k}{\pi}}\left[\left\{\frac{T_s(t)-T_s(0)}{\sqrt{t}}\right\}+\frac{1}{2}\int_0^t \frac{T_s(t)-T_s(\tau)}{(t-\tau)^{3/2}}d\tau\right] \tag{8}$$

The integral term in Eq. (8) can be expressed as summation forms by assuming a linear variation of the temperature between each measurement separated by the time step, Δt. Then, the conductive heat flux at a time t_n, n time steps after initial time t_0, is as follows [29, 30]:

$$\dot{q}_{cond}(t_n)=\sqrt{\frac{\rho c k}{\pi}}\left\{\frac{T_s(t_n)-T_s(t_0)}{\sqrt{t_n}}+\sum_{i=1}^{n-1}\left[\frac{T_s(t_n)-T_s(t_i)}{(t_n-t_i)^{\frac{1}{2}}}-\frac{T_s(t_n)-T_s(t_{i-1})}{(t_n-t_{i-1})^{\frac{1}{2}}}+2\frac{T_s(t_i)-T_s(t_{i-1})}{(t_n-t_i)^{1/2}+(t_n-t_{i-1})^{1/2}}\right]+\frac{T_s(t_n)-T_s(t_{n-1})}{\sqrt{\Delta t}}\right\} \tag{9}$$

However, the above equation, based on a one-dimensional assumption, is not valid in the region around the injection hole. As the low temperature sonic jet flows inside the hole and cools the inner hole surface, the conduction in this region occurs in a three-dimensional manner. This leads to an additional temperature drop near the injection hole, depicted as the black line in Fig. 5. Because heat flux is deduced by the temperature drop from an initial temperature, a measured heat flux would be

higher compared to an actual heat flux on the surface, shown by comparison between the red line and the blue line in Fig. 5. Therefore, care should be taken in deducing heat flux near the injection hole.

- **Added reference in revised manuscript**

[29] Alan Pope and Kenneth L. Goin. “High-speed wind tunnel testing.”, Wiley (1965)

[30] Henshall, B. D., and D. L. Schultz. "Some notes on the use of resistance thermometers for the measurement of heat transfer rates in shock tubes." (1959).

Comment (3)

Oil film visualization is not clear enough. There are some references that reveals clear structures in the near wall region by oil flow experiments. (e.g. Acta Astronautica, 2018, 148: 12-21. Acta Astronautica, 2020,168: 242-248. Acta Astronautica, 2018, 151: 886-892.) Authors should provide comments on that and emphasize novelty of their findings.

Answer to Comment (3)

The main objective of this study is heat transfer analysis, and the oil film visualization was performed to understand how the flow characteristics affect surface heat transfer augmentation. It means that the windward flow structure is more important than the leeward flow structure. For this reason, we try to distinguish the 1st and 2nd separations, which is enough to understand the thermo-fluidic behaviors near the hole in the study. However, as the reviewer pointed out, the picture of oil film visualization is not clear enough compared to the references. References provide clear oil film visualization so that leeward side of the jet flow structures such as V-shape separation zone, reflected shock and flow reattachment are clearly identified. In addition, references provide Nanoparticle-based Planar Laser Scattering (NPLS) image that shows detailed flow structures. Therefore, references have been added to the manuscript to make revised manuscript more comprehensive for understanding general authors in the journal.

- **Revised sentences in revised manuscript (page 10)**

In order to understand how the flow affects surface heat transfer, oil film is used to visualize flow structure on the surface. Carbon particles are mixed with a silicon oil to control the viscosity of the oil and to enhance a visibility of the surface streamline. The mixture is applied to the surface of the test plate and distributions of the film are taken after a wind tunnel run with camera.

- **Added sentences in revised manuscript (page 12)**

This flow phenomena could be better understood through more detailed oil film visualization results [32-34].

- **Added reference in revised manuscript**

[32] Liang, Chang-hai, et al. "Shock wave structures in the wake of sonic transverse jet into a supersonic crossflow." Acta Astronautica 148 (2018): 12-21.

[33] Liang, Chang-hai, et al. "Experimental study of parallel injections with different distances into a supersonic crossflow." Acta Astronautica 168 (2020): 242-248.

[34] Liu, Yuan, et al. "Structures of near-wall wakes subjected to a sonic jet in a supersonic crossflow." Acta Astronautica 151 (2018): 886-892.

Comment (4)

The analysis of flow structures should be added. Some paper on this topic can be cited in the introduction to make it more comprehensive. (Journal of Fluid Mechanics, 850, 551-583. AIAA Journal 2018 56:3, 1047-1059)

Answer to Comment (4)

As the reviewer pointed out, the analysis of flow structures was insufficient, which is very important to understand the flow characteristics of sonic jet in supersonic crossflow. In the previous manuscript, only the near wall counter rotating vortices which are the main factor in surface heat transfer, were mentioned. More detailed flow analysis is added to the introduction to make revised manuscript more comprehensive.

- **Added sentences in revised manuscript (page 4)**

The mechanism of formation of counter rotating vortices (CRVs) around the jet has also been well described. Viti et al. [21] identified six primary vortices: (i) horseshoe vortex, (ii) an upper trailing vortex, (iii) two trailing vortices formed in the separation region and, after of the bow shock wave, (iv) two more trailing vortices that eventually merge together into one single rotational motion. They found that three pairs of trailing counter rotating vortices (the second of iii and iv) merged into the kidney-shaped major CRVs downstream of the hole. M. B. Sun [22, 23] gave an analysis on the formation of trailing CRVs around the transverse jet with direct numerical simulation. The formation mechanism of the surface trailing CVPs are provided with the instantaneous and time-averaged flow structure [22]. They also found that as the flow penetrating the lateral side of the Mach disk where the strong shear condition exists, the baroclinic torque induces upper vorticities in the opposite rotating direction against the major CRVs [23].

- **Added reference in revised manuscript**

[21] Viti, Valerio, Reece Neel, and Joseph A. Schetz. "Detailed flow physics of the supersonic jet interaction flow field." Physics of fluids 21.4 (2009): 046101.

[22] Sun, Mingbo, and Zhiwei Hu. "Formation of surface trailing counter-rotating vortex pairs downstream of a sonic jet in a supersonic cross-flow." Journal of Fluid Mechanics 850 (2018): 551-583.

[23] Sun, Ming-Bo, and Z. W. Hu. "Generation of upper trailing counter-rotating vortices of

a sonic jet in a supersonic crossflow." AIAA Journal 56.3 (2018): 1047-1059.

Response to the 2nd reviewer's comments:

We appreciate the significant efforts that reviewers put into our paper to review. We will respond to the reviewer's comments and suggestions in detail in the following. According to the reviewer's opinion, we modified the manuscript with notification by highlighting and attached a full list of changes.

Comment (1)

In the introduction, the author needs to update the literatures to prove the study of the heat transfer near the injection hole is of great significance. However, the cited literatures are relatively old and cannot well prove the innovativeness of the article.

Answer to Comment (1)

As the reviewer pointed out, the cited literatures on the surface heat transfer analysis are relatively old compared to the literatures on flow analysis. After receiving the review, authors checked the recent research on heat transfer again, but authors could not find any recent literatures related to the surface heat transfer near the hole. However, the authors agreed that the necessity and innovation of this research should be clearly clarified. Therefore, the introduction is revised to emphasize the innovativeness of the article on page 4.

The flow physics of interaction between sonic jet and supersonic crossflow is applied to various systems, such as thrust vector control of supersonic vehicles, fuel injection in scramjet combustor. Recent studies have mainly focused on fuel combustion in scramjet combustor and analyzed flow structure, mixing and combustion characteristics. Measurement techniques such as a pressure-sensitive paint (PSP) and a particle image velocimetry (PIV) have enabled a detailed understanding of the flow structure on the surface and the characteristic of the mixing layer between the jet and the crossflow [15, 16]. Researches based on the large eddy simulation (LES) also contributed to an understanding of the flow by capturing the key characteristics of the large-scale structure of the mixing layer [17-20]. The mechanism of formation of counter rotating vortices (CRVs) around the jet has also been well described. Viti et al. [21] identified six primary vortices: (i) horseshoe vortex, (ii) an upper trailing vortex, (iii) two trailing vortices formed in the separation region and, after of the bow shock wave, (iv) two more trailing vortices that eventually merge together into one single rotational motion.

They found that three pairs of trailing counter rotating vortices (the second of iii and iv) merged into the kidney-shaped major CRVs downstream of the hole. M. B. Sun [22, 23] gave an analysis on the formation of trailing CRVs around the transverse jet with direct numerical simulation. A review by Huang [24] comprehensively summarized efforts to understand the flow and mixing characteristics caused by the interaction between the jet and the crossflow. Of course, it is very important to analyze the mixing and combustion characteristics in a high-speed flow to burn fuel efficiently within a limited supersonic combustion chamber length. However, it is also very important to analyze the heat transfer characteristics on the surface near the injected jet as their working gases are in high temperature and induce high heat transfer to component. Especially, the surface near the injection hole is a harsh region where severe heat transferred to a component. However, the number of published literatures related to this is very limited, and data for designing the system and validating numerical result are insufficient. There are few literatures that have studied the heat transfer on the surface where sonic jet injected into supersonic crossflow. Previously, Roberts et al. [25] measured heat transfer characteristics on the surface with a laminar hypersonic crossflow and a sonic jet using a thermo-liquid crystal (TLC) technique. However, TLC remains inactive in the near-hole region affected by the jet. Guelhan et al. [26] and Taguchi et al. [27] also measured heat transfer on a conical body with sonic jet under a hypersonic condition using infrared thermography. However, they utilized the assumption of a one-dimensional conduction on the surface and data around the hole is omitted. In the surface near the hole, the 1-D conduction assumption is not valid as the sonic jet flows inside the hole and heat transferred through the inner hole surface (see figure 5). Therefore, the conduction in this region occurs in a three-dimensional manner. This leads to an additional surface temperature change near the injection hole. Because heat flux is deduced by the temperature change from an initial temperature, a measured heat flux would be different compared to an actual heat flux on the surface. Consequently, an accurate measurement of the heat transfer near the injection hole is required to understand the characteristics of the heat transfer near the injection hole. Therefore, care should be taken in deducing heat flux near the injection hole.

In this study, a three-dimensional finite volume calculation was carried out with measured temperature distribution as a Dirichlet boundary condition. By using this method, a three-dimensional

conduction effect from the injection hole is taken into account, and the effect of the oscillatory behavior near the injection hole on the heat transfer is analyzed. The heat transfer results are analyzed in terms of a heat transfer coefficient and an adiabatic wall temperature, derived from the time history of heat flux and wall temperature.

- **Revised sentences in revised manuscript (page 4)**

Although several studies have been carried out in terms of flow structures and mixing characteristics, a little attention has been given to the heat transfer characteristic on the surface near the injected jet. However, this subject is critical in both scramjet combustor and thrust vector control of a missile as their working gases are in high temperature and can induce a high heat transfer to a component. Especially, the surface near the hole is a harsh region where severe heat transferred to a component as the region is affected by an oscillatory behavior of a shock structure [17]. The oscillation is provoked by a pressure fluctuation in the mixing layer when an ejection of the large-scale vortex occurs and results in oscillations of both barrel shock and bow shock. As the shock structure oscillates, the upstream recirculation region and vortices from it change and affect the heat transfer characteristics. Despite the importance of this subject, the number of published literatures related to this are very limited, and the data for designing the system and validating numerical result are insufficient. There are few literature that have studied the heat transfer on the surface where sonic jet injected into supersonic crossflow. Previously, Roberts et al. [25] measured heat transfer characteristics on the surface with a laminar hypersonic crossflow and a sonic jet using a thermo-liquid crystal (TLC) technique. However, TLC remains inactive in the near-hole region affected by the jet. Guelhan et al. [26] and Taguchi et al. [27] also measured heat transfer on a conical body with sonic jet under a hypersonic condition using infrared thermography. However, they utilized the assumption of a one-dimensional conduction on the surface and data around the hole is omitted. In the surface near the hole, the 1-D conduction assumption is not valid as the sonic jet flows inside the hole and heat transferred through the inner hole surface. Therefore the conduction in this region occurs in a three-dimensional manner. This leads to an additional surface temperature change near the injection hole. Because heat flux is deduced by the temperature change from an initial temperature, a measured heat flux would be different compared to an actual heat

flux on the surface. Consequently, an accurate measurement of the heat transfer near the injection hole is required to understand the characteristics of the heat transfer near the injection hole. Therefore, care should be taken in deducing heat flux near the injection hole.

In this study, a heat transfer near the injection hole caused by an interaction of a jet and a supersonic crossflow was measured using an infrared thermography. A sonic jet with different momentum ratios (J = 0.5, 1.0 and 1.5) was injected into a crossflow with Mach number of 3.0 developing through a length of 60 mm from a leading edge of a test plate. Heat flux distribution on the surface was inversely calculated from a time history of temperature measured in 60 Hz with an infrared camera. A three-dimensional finite volume calculation was carried out with measured temperature distribution as a Dirichlet boundary condition. By using this method, a three-dimensional conduction effect from the injection hole is taken into account, and the effect of the oscillatory behavior near the injection hole on the heat transfer is analyzed. The heat transfer results are analyzed in terms of a heat transfer coefficient and an adiabatic wall temperature, derived from the time history of heat flux and wall temperature.

Comment (2)

In section 2.3, all the assumptions can be explained in a unified way, and then the equation can be deduced and explained. It's easier to understand.

Answer to Comment (2)

The authors appreciate the reviewer's suggestion. The description of the reduction of heat flux and heat transfer coefficient in the previous manuscript was complicated and difficult to understand. Therefore, section 2.3 was revised in consideration of reviewer's comments and references are added to make manuscript easy to understand. In addition, nomenclature that was missing from the previous manuscript was added to page 2.

- **Added and revised sentences in revised manuscript (page 8)**

A convective heat flux on the surface is considered to be the same as a conductive heat flux into a solid. As the surface temperature is below room temperature, cooled from 295 K to 275 K during a measurement, the radiative heat flux at the surface can be neglected. A common practice for determination of the convective heat flux is considering the heat flux balance on the model surface locally in one-dimension. Given the low heat conductivity material such as Teflon, lateral conduction is negligible and semi-infinite solid approximation is valid during the testing time. At any point of the surface, the heat flux is

$$\dot{q}_{cond} = \dot{q}_{conv} = h(T_{aw} - T_s) \quad (4)$$

Where $\dot{q}_{cond}$ is conductive heat flux, $\dot{q}_{conv}$ denotes convective heat flux, h is convective heat transfer coefficient, T_{aw} and T_s are adiabatic wall temperature and surface temperature, respectively.

In addition, a change of a solid temperature due to the surface heat flux is governed by a three-dimensional energy conservation equation as described below:

$$\frac{\partial^2 T}{\partial x^2} + \frac{\partial^2 T}{\partial y^2} + \frac{\partial^2 T}{\partial z^2} = \frac{1}{\alpha}\frac{\partial T}{\partial t} \quad (5)$$

Assuming a one-dimensional heat transfer in an in-depth direction from the surface, while neglecting a lateral conduction, following equations are valid:

$$\frac{\partial^2 T}{\partial x^2} \ll \frac{1}{\alpha}\frac{\partial T}{\partial t} \quad and \quad \frac{\partial^2 T}{\partial y^2} \ll \frac{1}{\alpha}\frac{\partial T}{\partial t} \tag{6}$$

$$\frac{\partial^2 T}{\partial z^2} = \frac{1}{\alpha}\frac{\partial T}{\partial t} \tag{7}$$

When the semi-infinite solid approximation is valid, and the conduction occurs only in the in-depth direction, the conductive heat flux into a solid at a time t can be deduced from a time history of the surface temperature.

$$\dot{q}_{cond}(t) = \sqrt{\frac{\rho c k}{\pi}}\left[\left\{\frac{T_s(t) - T_s(0)}{\sqrt{t}}\right\} + \frac{1}{2}\int_0^t \frac{T_s(t) - T_s(\tau)}{(t-\tau)^{3/2}} d\tau\right] \tag{8}$$

The integral term in Eq. (8) can be expressed as summation forms by assuming a linear variation of the temperature between each measurement separated by the time step, Δt. Then, the conductive heat flux at a time t_n, n time steps after initial time t_0, is as follows [29, 30]:

$$\dot{q}_{cond}(t_n) = \sqrt{\frac{\rho c k}{\pi}}\left\{\frac{T_s(t_n) - T_s(t_0)}{\sqrt{t_n}} + \sum_{i=1}^{n-1}\left[\frac{\frac{T_s(t_n) - T_s(t_i)}{(t_n - t_i)^{\frac{1}{2}}} - \frac{T_s(t_n) - T_s(t_{i-1})}{(t_n - t_{i-1})^{\frac{1}{2}}}}{+2\frac{T_s(t_i) - T_s(t_{i-1})}{(t_n - t_i)^{1/2} + (t_n - t_{i-1})^{1/2}}}\right] + \frac{T_s(t_n) - T_s(t_{n-1})}{\sqrt{\Delta t}}\right\} \tag{9}$$

However, the above equation, based on a one-dimensional assumption, is not valid in the region around the injection hole. As the low temperature sonic jet flows inside the hole and cools the inner hole surface, the conduction in this region occurs in a three-dimensional manner. This leads to an additional temperature drop near the injection hole, depicted as the black line in Fig. 5. Because heat flux is deduced by the temperature drop from an initial temperature, a measured heat flux would be higher compared to an actual heat flux on the surface, shown by comparison between the red line and the blue line in Fig. 5. Therefore, care should be taken in deducing heat flux near the injection hole.

In this research, the three-dimensional transient energy equation of Eq. (5) is solved based on the finite volume method to accurately measure the heat transfer near the injection hole. The overall deduction procedure of a heat flux is shown in Fig. 6. First, measured IR images are interpolated into a computational surface grid by a least square interpolation for each time step. The interpolated surface temperatures are used as Dirichlet boundary conditions at each time for the finite volume calculation.

A boundary condition for the surface inside the hole is calculated by CFD simulation of the flow with a Mach number of 1.0 and a total pressure corresponding to each momentum ratio. For the CFD of the flow inside the hole, SST k-ω turbulence model was used in two-dimensional domain. The structured grids having 0.1 million elements were selected based on the grid independence test, and the height of the first cell near the wall was set to get wall y+ less than 1. The calculated heat transfer coefficient inside the hole, h_h, is assumed to be constant in time and h_h and $T_{aw,h}/T_0$ deduced from the CFD simulation are applied as a mixed boundary condition. In addition, all other walls including lower side of the Teflon block is assumed to be adiabatic. With these boundary conditions, a transient conduction in the Teflon block of the test plate with a thickness of 5 mm is solved with 1.1 million computational cells and a time step of 0.01667 sec (as surface temperature is taken with 60 Hz). All spatial and temporal gradients are discretized with 2nd-order implicit scheme and the heat flux on the surface, $\dot{q}_{conv}(t)$, at each time step is deduced.

- **Added sentences in revised manuscript (page 2)**

Nomenclature

J = jet-to-freestream momentum ratio
ρ = density
v = velocity
γ = specific heat ratio
p = pressure
M = Mach number
q_{cond} = conductive heat flux
q_{conv} = convective heat flux
h = heat transfer coefficient
T = Temperature
θ = temperature difference
z = depth
α = thermal diffusivity
c = specific heat capacity
k = thermal conductivity
t = time
D = diameter of injection hole
h_{aug} = augmentation of heat transfer coefficient
A_{pixel} = area of a pixel

Subscripts

j = jet exit property
∞ = freestream property
aw = adiabatic wall condition
s = surface property
0 = stagnation condition
h = injection hole property

- **Added references in revised manuscript**

[29] Alan Pope and Kenneth L. Goin. “High-speed wind tunnel testing.”, Wiley (1965)

[30] Henshall, B. D., and D. L. Schultz. "Some notes on the use of resistance thermometers for the measurement of heat transfer rates in shock tubes." (1959).

Comment (3)

Briefly explain the phenomenon under different momentum ratios（section 3.2).

Answer to Comment (3)

The momentum ratio of the jet to the crossflow, J is the dominant parameter determining the flow features of sonic jet and crossflow interaction. This parameter is given by the following expression:

$$J = \frac{\rho_j v_j^2}{\rho_\infty v_\infty^2} = \frac{\gamma_j\, p_j M_j^2}{\gamma_\infty\, p_\infty M_\infty^2}$$

The subscripts j and ∞ stand for jet and crossflow, respectively. With controlling the pressure of the jet, the momentum ratio of the jet and crossflow is controlled as the Mach number of the jet and crossflow are not changed in this study. The flow conditions for the test at each momentum ratio are summarized in table 1.

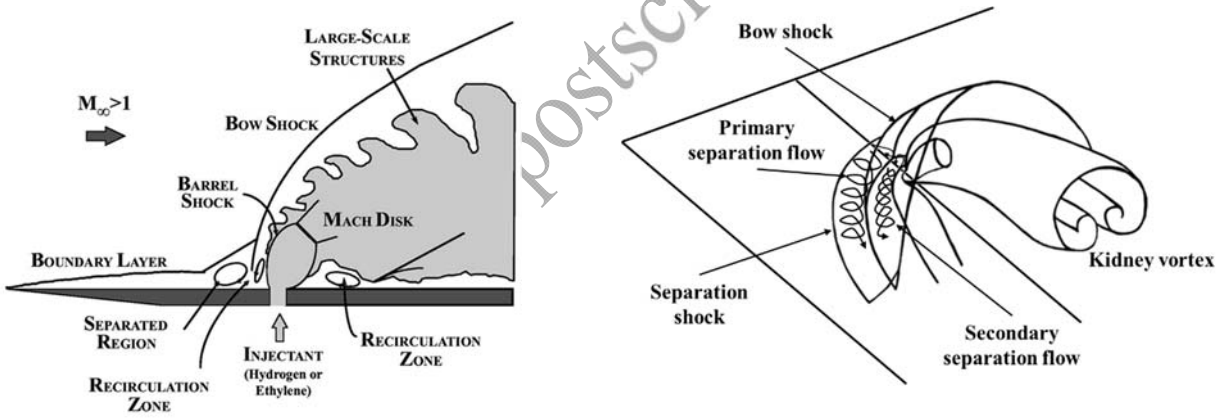

(a) Typical structure of flow filed with supersonic crossflow/sonic jet interaction [8]

(b) Trails of separated flow around the injection hole

Figure R1. Schematics of the flow field with a sonic jet and supersonic crossflow

Because the momentum of the jet acts as an obstacle to the supersonic crossflow, a bow shock develops in front of the jet (see figure R1). The under-expanded jet keeps accelerating downstream until it forms a Mach disk. Turning of the jet towards downstream direction is achieved by a barrel shock surrounding the jet plume. A mixing layer between the crossflow past the bow shock and the jet forms a large-scale structure around the trail of the jet. In addition, surface flow structure and heat transfer on the surface are strongly affected by the bow shock. Because of an adverse pressure gradient caused by the bow shock, the crossflow is separated in front of the bow shock. As a result, a separation shock called a 'Lambda shock' forms above the separation region, and an upstream recirculation region develops between the separation region and the injection hole by the pressure gradient around the jet. Two horseshoe vortices originating from these regions move around the injection hole to a downstream region, dominating a characteristic of the heat transfer on the surface.

As the momentum of the jet increases, jet acts as a larger and stronger obstacle to the crossflow. The barrel shock, bow shock and lambda shock develops on a larger scale [36], and the boundary layer separation is moved upstream. The size of recirculation region induced by the interaction between the bow shock and upstream boundary layer of jet also becomes larger [37].

In terms of heat transfer, figure 10 shows the distributions of the heat transfer coefficient and normalized adiabatic wall temperature with three different momentum ratios. As the momentum ratio increases, considerable phenomena regarding surface heat transfer coefficient have been observed. Firstly, the area affected by jet and crossflow interaction become wider in a spanwise direction, which is related to both the separation and recirculation of crossflow. Secondly, there is a notable change in the heat transfer at the trail of recirculation vortex as it significantly extends to the downstream region in a case with a higher momentum ratio. Thirdly, the jet separation region behind the hole, where it shows low heat transfer coefficient, also extends farther downstream because the flow separation behind the hole become more severe as the momentum of the jet increases. Finally, for all momentum ratios, the maximum heat transfer is caused by the oscillatory behavior in the vicinity of the hole and the

augmentation of the heat transfer by the oscillation does not show a significant change according to the momentum ratio either in terms of area or magnitude.

The magnitude of the temperature recovery by the upstream shock waves is similar for all three cases, as shown in the lower half of Fig. 10. The location and the strength of the bow shock does not vary significantly, while the separation shock (Lambda shock) becomes wider in a spanwise direction at high momentum ratio. At the downstream of the injection hole, the temperature recovery of the $J = 0.510$ case shows a different pattern compared to those of the other cases. It seems that the effect of the reattachment of the jet and a reflected shock wave is weak, as the jet separation region downstream of the hole is small in the $J = 0.510$ case. Therefore, the temperature at the downstream is recovered quickly in the $J = 0.510$ case, compared to the other cases. On the other hand, the effect of the reattachment of the jet and the shock reflection from the reattachment point is clearly visible in $J = 1.018$ and $J = 1.477$ cases.

- **Revised sentences in revised manuscript (page 14)**

As the momentum of the jet increases, jet acts as a larger and stronger obstacle to the crossflow. The barrel shock, bow shock and lambda shock develops on a larger scale [36], and the boundary layer separation is moved upstream. The size of recirculation region induced by the interaction between the bow shock and upstream boundary layer of jet also becomes larger [37].

In terms of heat transfer, figure 10 shows the distributions of the heat transfer coefficient and normalized adiabatic wall temperature with three different momentum ratios. As the momentum ratio increases, considerable phenomena regarding surface heat transfer coefficient have been observed. Firstly, the area affected by jet and crossflow interaction become wider in a spanwise direction, which is related to both the separation and recirculation of crossflow. Secondly, there is a notable change in the heat transfer at the trail of recirculation vortex as it significantly extends to the downstream region in a case with a higher momentum ratio. Thirdly, the jet separation region behind the hole, where it shows low heat transfer coefficient, also extends farther downstream because the flow separation behind the hole become more severe as the momentum of the jet increases. Finally, for all momentum ratios,

the maximum heat transfer is caused by the oscillatory behavior in the vicinity of the hole and the augmentation of the heat transfer by the oscillation does not show a significant change according to the momentum ratio either in terms of area or magnitude.

- **Added reference in revised manuscript**

[36] Génin, Franklin, and Suresh Menon. "Dynamics of sonic jet injection into supersonic crossflow." Journal of Turbulence 11 (2010): N4.

[37] Zhao, Majie, et al. "Study of sonic injection from circular injector into a supersonic cross-flow using large eddy simulation." International journal of hydrogen energy 41.39 (2016): 17657-17669.

Comment (4)

The conclusion indicates the significance and purpose of the paper：the augmentation of heat transfer near the injection hole should be considered properly. This conclusion is too general. Through the study of this paper, can it further guide the thermal design process of systems with similar flow physics，how to design ?

Answer to Comment (4)

As the reviewer commented, the authors agreed that the conclusion of the previous manuscripts was too general, and the importance of this study cannot be emphasized well. Therefore, the conclusion of previous manuscript was revised on page 17 as below;

- **Revised sentences in revised manuscript (page 17)**

The resulting augmentation of heat transfer in the jet interaction area compared to the freestream value was found to be changed from 159% to 192%. Furthermore, the augmentation of heat transfer at the near-hole area was at least 390% at the low momentum ratio and could increase up to 503% with J = 1.477. Therefore, the augmentation of heat transfer near the injection hole should be considered properly. When thermal designing a system with similar flow physics, the type and thickness of composite material [38] should be chosen considering the augmentation of heat transfer near the hole. Appling titanium or abrasives locally to the wall near the injection hole could be a way to protect the thermal components.

- **Added reference in revised manuscript**

[38] Choubey, Gautam, Lakka Suneetha, and K. M. Pandey. "Composite materials used in Scramjet-A Review." Materials Today: Proceedings 5.1 (2018): 1321-1326.